

# Variability of Jupiter's main auroral emission and satellite footprints observed with HST during the Galileo era

Marissa F. Vogt<sup>1</sup>, Matthew James Rutala<sup>1</sup>, Bertrand Bonfond<sup>2</sup>, John T. Clarke<sup>1</sup>, Luke Moore<sup>1</sup>, and Jonathan D. Nichols<sup>3</sup>

<sup>1</sup>Boston University

<sup>2</sup>Université de Liège

<sup>3</sup>University of Leicester

November 22, 2022

## Abstract

Hubble Space Telescope images of Jupiter's UV aurora show that the main emission occasionally contracts or expands, shifting toward or away from the magnetic pole by several degrees in response to changes in the solar wind dynamic pressure and Io's volcanic activity. When the auroral footprints of the Galilean satellites move with the main emission this indicates a change in the stretched field line configuration that shifts the ionospheric mapping of a given radial distance at the equator. However, in some cases, the main emission shifts independently from the satellite footprints, indicating that the variability stems from some other part of the corotation enforcement current system that produces Jupiter's main auroral emissions. Here we analyze HST images from the Galileo era (1996-2003) and compare latitudinal shifts of the Ganymede footprint and the main auroral emission. We focus on images with overlapping Galileo measurements because concurrent measurements are available of the current sheet strength, which indicates the amount of field line stretching and can influence both the main emission and satellite footprints. We show that the Ganymede footprint and main auroral emission typically, but do not always, move together. Additionally, we find that the auroral shifts are only weakly linked to changes in the current sheet strength measured by Galileo. We discuss implications of the observed auroral shifts in terms of the magnetospheric mapping. Finally, we establish how the statistical reference main emission contours vary with CML and show that the dependence results from magnetospheric local time asymmetries.

1 **Variability of Jupiter’s main auroral emission and satellite footprints observed with HST**  
2 **during the Galileo era**

3 Marissa F. Vogt<sup>1</sup>, Matthew Rutala<sup>1,2</sup>, Bertrand Bonfond<sup>3</sup>, John T. Clarke<sup>1,2</sup>, Luke Moore<sup>1</sup>, and  
4 Jonathan D. Nichols<sup>4</sup>

5 <sup>1</sup> Center for Space Physics, Boston University, Boston, MA, USA

6 <sup>2</sup> Department of Astronomy, Boston University, Boston, MA, USA

7 <sup>3</sup> Space sciences, Technologies and Astrophysics Research (STAR) Institute, LPAP, Université  
8 de Liège, Liège, Belgium

9 <sup>4</sup> Department of Physics and Astronomy, University of Leicester, Leicester, UK

10

11 Corresponding author: Marissa Vogt, mvogt@bu.edu

12

13 **Abstract**

14 Hubble Space Telescope images of Jupiter’s UV aurora show that the main emission  
15 occasionally contracts or expands, shifting toward or away from the magnetic pole by several  
16 degrees in response to changes in the solar wind dynamic pressure and Io’s volcanic activity.  
17 When the auroral footprints of the Galilean satellites move with the main emission this indicates  
18 a change in the stretched field line configuration that shifts the ionospheric mapping of a given  
19 radial distance at the equator. However, in some cases, the main emission shifts independently  
20 from the satellite footprints, indicating that the variability stems from some other part of the  
21 corotation enforcement current system that produces Jupiter’s main auroral emissions. Here we  
22 analyze HST images from the Galileo era (1996-2003) and compare latitudinal shifts of the  
23 Ganymede footprint and the main auroral emission. We focus on images with overlapping

24 Galileo measurements because concurrent measurements are available of the current sheet  
25 strength, which indicates the amount of field line stretching and can influence both the main  
26 emission and satellite footprints. We show that the Ganymede footprint and main auroral  
27 emission typically, but do not always, move together. Additionally, we find that the auroral shifts  
28 are only weakly linked to changes in the current sheet strength measured by Galileo. We discuss  
29 implications of the observed auroral shifts in terms of the magnetospheric mapping. Finally, we  
30 establish how the statistical reference main emission contours vary with CML and show that the  
31 dependence results from magnetospheric local time asymmetries.

32

### 33 **Plain Language Summary**

34 Jupiter's main auroral emission is thought to be the result of a current system that develops to  
35 help circulate plasma from Io as it moves through Jupiter's magnetosphere. There are many  
36 factors that can influence the position and brightness of Jupiter's main emission, including the  
37 solar wind and internal factors like Io's volcanic activity. The auroral footprints of Jupiter's  
38 moons Io, Europa, and Ganymede can provide important clues to what factors influence  
39 variability in the main auroral emission because some processes, like those that affect the radial  
40 stretching of the magnetic field, will affect the position of both the satellite footprints and the  
41 main emission. In this study we quantify and compare variability in the position of Jupiter's main  
42 auroral emission and the Ganymede footprint in images from the Hubble Space Telescope. We  
43 focus on images from the Galileo era (1996-2003) and compare variability in the auroral  
44 emissions to Galileo observations of magnetospheric variability. We find that the Ganymede  
45 footprint and main auroral emission typically change in the same way, but find the expected  
46 relationship between the auroral motion and the magnetic field measured by Galileo to be weak.

47 **1. Introduction**

48           It has been nearly 30 years since the Hubble Space Telescope took its first images of  
49 Jupiter's aurora with its Faint Object Camera (Caldwell et al., 1992). Subsequent high resolution  
50 images with HST's WFPC-2 (Wide Field Planetary Camera 2), ACS (Advanced Camera for  
51 Surveys), and STIS (Space Telescope Imaging Spectrograph) instruments have shown that  
52 Jupiter's ultraviolet auroral emissions can be classified into three types. From most equatorward  
53 to poleward, they are: the equatorward emissions, which include auroral injection signatures and  
54 the magnetic footprints of the Galilean satellites Io, Europa, Ganymede, and Callisto; the main  
55 auroral emission, a relatively constant and narrow ( $\sim 1-3^\circ$  latitudinal width) band of emissions  
56 forming a kidney bean shape in the northern hemisphere and an oval in the south; and the polar  
57 emissions, which are highly variable and include flares, spots, a dark region, and arc-like  
58 features.

59           Jupiter's main auroral emission is thought to be the result of a corotation enforcement  
60 current (CEC) system that arises due to the breakdown of plasma corotation in the middle  
61 magnetosphere (Cowley and Bunce, 2001; Hill, 2001). The primary source of plasma in Jupiter's  
62 magnetosphere is the moon Io, whose volcanic activity adds plasma to the system at a rate of  
63  $\sim 500-1000$  kg/s (Thomas et al., 2004). As plasma diffuses radially outward from its source at  
64 Io's orbit (5.9 Jovian radii or  $R_J$ ;  $1 R_J = 71,492$  km) its azimuthal velocity decreases to conserve  
65 angular momentum, and a CEC system develops. The plasma is accelerated back up toward  
66 corotation by a  $\mathbf{j} \times \mathbf{B}$  force provided by the radially outward current, and the upward (out of the  
67 ionosphere) field-aligned current, carried by downward moving electrons, is thought to produce  
68 the main auroral emission. Though the corotation enforcement theory for the production of  
69 Jupiter's main aurora has been widely accepted, Bonfond et al. (2020) recently highlighted

70 several pieces of observational evidence that are broadly inconsistent with the typical CEC  
71 description. Several recent observations and theoretical studies indicate that waves, including  
72 ULF (Pan et al. 2021, Lysak and Song, 2020), EMIC (Yao et al., 2021), Alfvén (Gershman et al.,  
73 2019; Saur et al., 2018), and whistler mode waves (Elliott et al., 2018), may play a larger role in  
74 the generation of the Jovian aurorae than previously foreseen. Any auroral origin theory must be  
75 ultimately able to account for observed auroral properties like brightness, position, and both  
76 temporal and spatial variability.

77         Though sometimes called the “main oval”, Jupiter’s main auroral emissions are actually  
78 shaped like a kidney bean in the northern hemisphere, as shown in the HST polar projections in  
79 Figure 1, due to the presence of a weak-field anomaly in the internal magnetic field (Grodent et  
80 al. 2008b). The southern main auroral emissions form an oval roughly centered on the southern  
81 magnetic pole, which is tilted by  $\sim 10^\circ$  with respect to the rotation axis. The main emission  
82 brightness ranges from tens to thousands of kiloRayleighs (kR) and varies temporally as well as  
83 with CML and local time (e.g. Grodent et al., 2003). Its morphology also varies with local time:  
84 the main emission width ranges from  $\sim 0.5^\circ$ - $1^\circ$  in the dawn to noon sector to as wide as  $\sim 3^\circ$  near  
85 dusk, and a “discontinuity” typically appears pre-noon (Radioti et al., 2008). The location of the  
86 main emission maps roughly to a source region at  $\sim 20$ - $40 R_J$  in the magnetosphere, which is  
87 consistent with the CEC theory (e.g. Nichols and Cowley, 2004; Nichols et al., 2020), though the  
88 mapping varies with local time (Vogt et al., 2011). The main emission occasionally contracts or  
89 expands, shifting toward or away from the magnetic pole, by several degrees (e.g. Grodent et al.,  
90 2008a; Nichols et al., 2009). This motion is often referred to as a “latitudinal shift” and is largely  
91 in the direction of magnetic, not jovigraphic, latitude, particularly in the northern hemisphere.  
92 This type of variability, which has been linked to both changes in the solar wind dynamic

93 pressure (Grodent et al., 2003) and changes internal to the magnetosphere like volcanic activity  
94 on Io or changes in the hot plasma pressure gradient (Bonfond et al., 2012; Nichols, 2011;  
95 Nichols et al., 2015), is the focus of our study.

96         There are two likely explanations for the observed latitudinal shifts of Jupiter's main  
97 auroral emission. The first is a change in the magnetic field configuration that shifts the  
98 ionospheric mapping of a given radial distance in the equatorial magnetosphere. For example, if  
99 a magnetospheric magnetic field line becomes more (less) radially stretched compared to its  
100 average state then its ionospheric footprint would shift equatorward (poleward) compared to its  
101 typical mapping, as illustrated in Figure 1 (top left). The figure illustrates why the ionospheric  
102 footprint of a fixed radial distance in the magnetosphere, such as Ganymede's orbit at 15  $R_J$ ,  
103 shifts equatorward as the field becomes increasingly radially stretched. In this illustration, the  
104 dashed outer blue field line (weak current sheet) and the solid inner red field line (strong current  
105 sheet) both cross the equator at the same radial distance but the ionospheric footprint of the  
106 dashed blue field line is poleward of the solar red field line. Additionally, the two solid field  
107 lines in the figure have the same ionospheric footprint, but the equatorial crossing point is much  
108 larger for the radially stretched red field lines (strong current sheet) than for the more dipolar  
109 blue field lines (weak current sheet). Therefore, a change in the magnetic field configuration can  
110 lead to a latitudinal shift of the main auroral emission by shifting the ionospheric footprints of  
111 field lines that are linked to the radial distance where the CEC system peaks. A change in the  
112 magnetic field configuration would also affect the latitudinal positions of the auroral satellite  
113 footprints since they are linked to a fixed orbital distance.

114         The second likely cause of latitudinal shifts in Jupiter's main auroral emission is a change  
115 in part of the CEC system that produces the main auroral emission, such as a change in the

116 plasma mass loading rate or in the radial profile of the plasma azimuthal velocity. These changes  
117 can alter the radial distance of the peak corotation enforcement currents, as shown in the  
118 magnetodisk modeling work of Nichols (2011) and Nichols et al. (2015), and latitudinally shift  
119 the main emission as its equatorial radial mapping changes. These changes may also lead to a  
120 shift in the satellite footprint locations, as the Nichols modeling work shows. However, in  
121 general, changes in the CEC system would not *necessarily* lead to a shift in the satellite footprint  
122 locations unless the field geometry also changed. For example, the Ganymede footprint is  
123 located close to its expected location in the auroral image reproduced in Figure 1 (bottom right),  
124 but the main auroral emission is so extremely expanded that it is located equatorward of the  
125 Ganymede footprint, indicating a magnetospheric source distance inside of  $15 R_J$  (Bonfond et al.,  
126 2012). The latitudinal motion of the satellite footprints is therefore a useful diagnostic tool for  
127 identifying the cause of latitudinal shifts in the main auroral emission.

128         In this paper we survey the HST auroral images from the Galileo era (1996-2003) and  
129 compare how latitudinal shifts of the Ganymede footprint compare to concurrent shifts in the  
130 main auroral emission, with the ultimate goal of furthering our understanding of how Jupiter's  
131 magnetosphere-ionosphere (M-I) coupling system varies in time. We focus on images with  
132 overlapping Galileo measurements because concurrent information is available about the amount  
133 of field line radial stretching, which can affect the position of both the main emission and  
134 satellite footprints (Vogt et al., 2017). We consider whether the main emission and satellite  
135 footprints occur independently and compare the auroral shifts to Galileo fits of the current sheet  
136 current density. Section 2 presents an overview of the data used in this study, section 3 describes  
137 how we identified the position of the main auroral emission and corrected for viewing geometry,  
138 and section 4 discusses our results and future work. We conclude in section 5 with a summary.

139

## 140 **2. Data used in this study**

141

### 142 2.1 HST data availability, image reduction, and limb fitting

143         In this study we use images taken with HST's STIS instrument, which has a resolution of  
144 0.0246 arcsec/pixel. We are interested in comparing auroral variability to changes measured in  
145 Jupiter's magnetosphere by the Galileo spacecraft, which orbited Jupiter from 1996 to 2003.  
146 Therefore, we began our analysis by looking at the 170 images that are available from 25 unique  
147 dates beginning in September 1996 and ending in February 2001. These images come from  
148 observing programs 7308, 7769, 8171, and 8657. Most of the images have been analyzed in  
149 some way in previous studies (e.g. Clarke et al., 2002; Grodent et al., 2003) but with a different  
150 focus than our present work. An additional 13 images are available from observing program  
151 9685 during 24-26 February 2003 (DOY 55-57), though the last Galileo magnetometer data  
152 available from Jupiter's magnetosphere are from November 2002, so we have excluded these  
153 from our study.

154         From the initial list of 170 images, we have excluded 27 images (13 from the northern  
155 hemisphere and 14 from the southern hemisphere) in which our analysis was unable to clearly  
156 identify a significant part of the main emission (see Section 3), almost always because of an  
157 unfavorable viewing geometry. Though the main emission is not circular, especially in the north  
158 hemisphere, it is still roughly centered on the magnetic pole in both hemispheres. Jupiter's  $\sim 10^\circ$   
159 dipole tilt, toward  $\sim 200^\circ$  System III (SIII) longitude (left handed), means that the visibility of the  
160 main emission is heavily biased for certain central meridian longitudes (CMLs). The 82 northern  
161 hemisphere images used in this study have CMLs ranging from  $\sim 90^\circ$  to  $\sim 290^\circ$  with a median of

162 ~180°, and the 61 southern hemisphere images used in this study have CMLs ranges of ~300°-  
163 360° and ~0°-120°. Table S1 lists the date, time, CML, and other relevant details for the 143  
164 images used in this study.

165 HST images were reduced following the latest version of the BU pipeline process (see  
166 Clarke et al., 2009). This process includes a dark count subtraction, flat field response correction,  
167 interpolation over bad pixels, and other corrections and rotations necessary to identify the planet  
168 center and make a polar projection of each image. The planetary limb fitting provides an  
169 uncertainty of up to a few pixels in the position of different auroral features. In order to mitigate  
170 the effects of this uncertainty on our analysis we consider the relative positions of the main  
171 auroral emission and Ganymede footprint in addition to the precise position or shift with respect  
172 to a fixed reference contour. In our image reduction we used the same planetary center pixel  
173 values as Bonfond et al. (2017) and confirmed that the satellite footprint locations we obtained  
174 matched the coordinates provided in their supplemental material. The Ganymede or Europa  
175 footprints were detected in roughly half of the 143 images used in this study: 62 images  
176 contained the Ganymede footprint (34 in the northern hemisphere and 28 in the southern  
177 hemisphere) and 7 images included the Europa footprint in the southern hemisphere. In our  
178 analysis we focus on the Ganymede footprints because there are so few images containing the  
179 Europa footprint and exclude three images (one from the northern hemisphere and two in the  
180 southern hemisphere) in which the Ganymede footprint is located very close to the limb of the  
181 planet, which makes it difficult to accurately characterize any shift of the footprint with respect  
182 to the reference footpath or the main emission.

183

184 2.2 Galileo data used in this study

185           The Galileo spacecraft completed over 30 orbits of Jupiter, surveying the magnetosphere  
186 at radial distances up to  $\sim 150 R_J$  and providing excellent coverage at nightside local times, as  
187 shown by the black orbit tracks in Figure 2. Colored boxes in Figure 2 show the spacecraft  
188 position at the times of all images used in this study excepting the two images from 28 May 1998  
189 (DOY 148), when Galileo was located in the predawn middle magnetosphere but no concurrent  
190 magnetometer data are available. Galileo was located inside of  $30 R_J$  for 32 of our 143 HST  
191 images, in the middle to outer magnetosphere for 76 images, and in the solar wind or  
192 magnetosheath for the remaining 35 images. For all images when Galileo was located in the solar  
193 wind or magnetosheath the spacecraft was located outside of the expanded Joy et al. (2002)  
194 magnetopause (outer light blue line in Figure 2).

195           Images from intervals when the spacecraft was located inside of  $30 R_J$  are particularly  
196 relevant because real-time information is available about Jupiter's current sheet and the degree of  
197 radial stretching in the magnetic field. Vogt et al. (2017) analyzed temporal variability in  
198 magnetometer data from radial distances  $10\text{-}30 R_J$  in each of Galileo's orbits. Specifically, they  
199 obtained an orbit-by-orbit fit of the Connerney, Acuña, and Ness (1981) current sheet model  
200 parameter  $\mu_0 I_0$ , the current sheet current density, which indicates the strength of the current sheet  
201 or the amount of radial field stretching. Larger values of  $\mu_0 I_0$  indicate a stronger current sheet  
202 and a more radially stretched field. The best fit  $\mu_0 I_0$  values are shown in the top panel of Figure  
203 3; we note that because the focus of Figure 3 is a comparison to the HST auroral images the time  
204 range of Figure 3 omits some Galileo  $\mu_0 I_0$  fits from 1996 to early 1997 and from late 2001 to  
205 2002. Error bars indicate variability in the inbound and outbound  $\mu_0 I_0$  fits of each orbit, though  
206 the  $\mu_0 I_0$  fit values were generally stable on the  $\sim 5\text{-}10$  day timescale during which the spacecraft  
207 was located at distances from  $10$  to  $30 R_J$ . Auroral mapping models show that the overall  $\mu_0 I_0$

208 variability would be expected to produce a  $\sim 2.3^\circ$  shift in the ionospheric position of model field  
209 lines traced from  $30 R_J$ , a  $\sim 1.5^\circ$  shift in the modeled Ganymede footprint location, and a  $\sim 0.7^\circ$   
210 shift in the modeled Io footprint location. The top right of Figure 1 shows an example of the  
211 expected auroral shifts in the northern ionosphere that would be consistent with the measured  
212 current sheet variability observed by Galileo, estimated by tracing model field lines with  
213 different current sheet parameters. Vogt et al. (2017) performed an initial analysis of 27 HST  
214 images with similar CMLs to examine how the size of the main “oval” changed with the  
215 contemporaneous best fit  $\mu_0 I_0$ , but did not find a clear relationship. Here we expand on that  
216 initial work on the main emission and also consider how the best fit  $\mu_0 I_0$  affects the observed  
217 locations of the satellite footprints.

218

### 219 **3. Analysis: main emission identification and CML correction**

220 Since Bonfond et al. (2017) have already identified the satellite footprint locations in our  
221 images, after confirming these locations the primary task in our analysis was to obtain the  
222 position of the main auroral emission. Figure 4 illustrates our approach using a northern  
223 hemisphere image from 25 November 1998 at a Central Meridian Longitude (CML) of  $164.2^\circ$ .  
224 We began by identifying “slices” of magnetic longitude, assuming the magnetic pole is located at  
225  $10.31^\circ$  latitude and  $196.61^\circ$  System III longitude (left handed) following the JRM09 field model  
226 (Connerney et al., 2018), with a resolution of  $2^\circ$  longitude. The thick colored lines emanating  
227 from the magnetic pole in the left panel of Figure 4 show some of these magnetic longitude  
228 slices, drawn every  $10^\circ$  in magnetic longitude.

229 Next, we identified the position where each magnetic longitude slice intersects with the  
230 Nichols et al. (2009) reference main emission, drawn in gray in Figure 4. We then obtained a

231 Gaussian fit to the auroral brightness along each magnetic longitude slice within the region that  
232 is  $\pm 4.5^\circ$  magnetic latitude from the reference main emission, outlined by the two pink contours in  
233 the left panel of Figure 4. The right panel of Figure 4 shows auroral brightness and Gaussian fits  
234 from selected magnetic longitude slices as a function of distance from the Nichols et al. (2009)  
235 reference contour, defined as positive for points poleward of the reference contour. The color of  
236 each line corresponds to the color of the magnetic longitude slice drawn in the left panel of  
237 Figure 4; for clarity we have only drawn lines every  $15^\circ$  of magnetic longitude. Finally, we  
238 identified the main emission location, plotted as white stars in Figure 4, as the position of the  
239 peak in the Gaussian fit on each magnetic longitude slice. We have confirmed that we obtain  
240 very similar main emission positions whether we use a Gaussian fit approach or whether we  
241 define the main emission location as the point of peak brightness along each magnetic longitude  
242 slice. The difference between the main emission points identified with the two different  
243 approaches was typically  $\sim 0.1^\circ$  in spherical distance and both approaches lead to very similar  
244 estimates of auroral variability.

245 In our analysis we exclude points where the main emission was misidentified (for  
246 example, because of a feature like the Ganymede footprint) or is sharply discontinuous.  
247 Therefore, there are some gaps in the main emission location stars shown in Figure 4. Many of  
248 these gaps occur in the auroral discontinuity region at pre-noon local times (Radioti et al., 2008)  
249 and in the northern auroral “kink” sector, where the main emission can be difficult to identify  
250 and often features multiple arcs. As previously mentioned, we discarded completely 26 images  
251 for which we were unable to obtain good fits to the main auroral emission, largely due to the  
252 viewing geometry.

253           Several previous authors have identified reference main emission contours by co-adding  
254 images (Grodent et al., 2003; Nichols et al., 2009; Bonfond et al., 2017). We take a slightly  
255 different approach here, defining a statistical reference main emission contour by identifying the  
256 average position of the main emission. For example, Figure 5 shows the distribution of the main  
257 emission positions along each magnetic longitude slice identified using the approach described  
258 above. Each box in Figure 5 has dimensions of  $2^\circ$  magnetic longitude by  $0.1^\circ$  magnetic latitude  
259 and its color indicates the number of images in which the main emission position, as identified  
260 by the peak of the Gaussian fit, was located within that box. The main emission locations are  
261 scattered by as much as  $\sim 3\text{-}4^\circ$  in magnetic latitude but are concentrated in narrow bands that are  
262 close to the Nichols et al. (2009) reference contour in the north and the Grodent et al. (2003)  
263 reference contour in the south (thick gray lines). The scatter in the main emission peak locations  
264 is generally largest near dusk and smallest near dawn, where the main emission tends to be  
265 narrow and well-defined in HST images. We define our reference contour by calculating the  
266 average magnetic latitude of the main emission in each magnetic longitude bin. Our resulting  
267 reference contours for the northern and southern hemispheres are shown by the thick black lines  
268 in Figure 5. Figure 6 shows that our statistical reference contours are similar in shape and  
269 location to the reference contours derived by Grodent et al. (2003), Nichols et al. (2009), and  
270 Bonfond et al. (2017). Our statistical reference contour most closely matches Grodent et al.  
271 (2003), as expected since that study and ours used a nearly identical set of images.

272           The main emission position varies with CML (Grodent et al., 2003), so we have also  
273 plotted the distribution of main emission positions separately for certain CML ranges in Figure 5  
274 and we have calculated CML-specific statistical reference main emission contours, which are  
275 plotted in the top panel of Figure 7. In the northern hemisphere we considered the following

276 CML ranges: CMLs 80°-140° (purple), 140°-190° (blue), 190°-240° (green), 240°-290° (red); in  
277 the southern hemisphere we considered CMLs 0°-60° (purple), 60°-180° (blue), and 290°-  
278 360° (red). (Note that there are no northern images with CMLs less than 80° or larger than 290°,  
279 and no southern hemisphere images with CMLs between 180° and 290°.) In the northern  
280 hemisphere, the main emission is most expanded at small CMLs (purple) and becomes more  
281 contracted with increasing CML (e.g. red contour), as noted by Grodent et al. (2003). The CML  
282 dependence is not as noticeable in the southern hemisphere as it is in the northern hemisphere,  
283 though again the reference contour at the earliest CMLs (red) is most expanded. This behavior in  
284 both hemispheres is consistent with the main emission shifting poleward at dusk compared to its  
285 average location for a given location, as we discuss in more detail in section 4.3.

286

## 287 **4. Results and Discussion**

288

### 289 *4.1 Comparison of main emission and satellite footprint shifts*

290 After identifying the main emission in each HST image we can now consider whether the  
291 main emission and satellite footprints shift independently or whether they demonstrate similar  
292 temporal behavior (i.e. whether poleward motion of the main emission is typically accompanied  
293 by poleward motion of the satellite footprints). For each image that contained a satellite footprint  
294 we define the Ganymede footprint shift as the minimum spherical distance between the observed  
295 satellite footprint and the reference footpath derived by Bonfond et al. (2017). Similarly, we  
296 define the main emission shift as the mean distance between the main emission and the CML-  
297 specific statistical reference contour (see section 3). For both the main emission and Ganymede

298 footprint we define the shift as positive if the relevant auroral feature is poleward of the reference  
299 contour/footpath and negative if it is equatorward.

300 Figure 8 shows plots of the Ganymede footprint shift and the main emission shift. This  
301 figure contains data from the 59 images (33 of the northern hemisphere and 26 of the southern  
302 hemisphere) for which the main auroral emission was clearly identified and the Ganymede  
303 footprint was not located close to the limb of the planet (see section 2.1). In the left panel we  
304 calculated the main emission shift using the main emission location at all longitudes; in the right  
305 panel we calculated the main emission shift using only the main emission points in the  $10^\circ$   
306 magnetic longitude bin (e.g.  $0^\circ$ - $10^\circ$ ,  $10^\circ$ - $20^\circ$ , etc.) closest to the Ganymede footprint. In both  
307 plots two thirds of the points are located in the upper right or lower left quadrants, indicating that  
308 the footprint and main emission shift together (both poleward or both equatorward). The linear  
309 correlation coefficient of the two shifts is stronger when considering the main emission shift only  
310 at magnetic longitudes near the Ganymede footprint (linear correlation coefficient 0.52) instead  
311 of at all longitudes (linear correlation coefficient 0.37). This could indicate that the processes that  
312 change the magnetic field configuration and produce auroral shifts are somewhat localized.

313 Of the images for which the Ganymede footprint and main emission shift separately,  
314 most come from the northern hemisphere and involve an equatorward motion of the main  
315 emission. Interestingly, in all four images from 26 July 1998 (DOY 207) the main emission was  
316 shifted equatorward while the Ganymede footprint was shifted poleward (all four images from  
317 this date are of the northern hemisphere). The images which feature opposite footprint and main  
318 emission shifts do not otherwise appear to be more likely to occur under specific conditions or  
319 circumstances like date, CML, footprint longitude, best fit magnetodisk parameter  $\mu_0 I_0$ , etc.

320 Overall, we conclude that the main emission and Ganymede footprint generally, but do  
321 not always, shift together. However, our conclusion comes with several caveats about the  
322 uncertainty of the planetary limb fitting / center pixel finding process, which affects the absolute  
323 shifts of both the main emission and Ganymede footprint. Due to the uncertainty in fitting the  
324 planet center in each HST image, Bonfond et al. (2017) assumed an uncertainty of 8 pixels,  
325 which typically corresponds to  $\sim 2^\circ$  spherical distance, in the footprint spot locations from STIS  
326 images. This uncertainty is larger than the typical auroral shifts we have calculated here but is  
327 likely an overestimate (a more typical assumed uncertainty value is  $\sim 3$  pixels). We can remain  
328 reasonably confident in our analysis since the uncertainty associated with the limb fitting applies  
329 to both the main emission and the Ganymede footprint, though exactly whether the uncertainty  
330 affects the footprint and main emission in the same way – for example, whether an  $n$ -pixel error  
331 in the planetary center finding shifts both the main emission and footprint poleward/equatorward  
332 or shifts them in opposite directions – depends on factors like the image CML, position of the  
333 auroral feature, and direction of the limb fitting error. Using a subset of representative images at  
334 a range of CMLs we calculated that a 3 pixel uncertainty in the planetary center pixel results in  
335 an typical variability in the main emission position of  $\sim 0.2^\circ$ - $0.8^\circ$ , with an average value of  $\sim 0.4^\circ$ .  
336 We note, that the time series in Figure 3 shows that the main emission shifts among images from  
337 the same day can vary significantly, sometimes even being of opposite sign. We do not believe  
338 this is indicative of a physical process – the timescale is likely too short – but probably reflects  
339 some of the error and uncertainty in our analysis, including the planet center pixel finding and  
340 main emission identification. Finally, we note that it is important to note that the Ganymede  
341 footpath which provides the basis for calculating the footprint shift was derived by Bonfond et al.  
342 (2017) using more images, and likely covering a wider range of magnetospheric conditions, than

343 we have considered in our study. Their dataset encompassed dates from 1997 to 2014 and  
344 included more than 700 images in the north and more than 200 images in the south.

345

#### 346 *4.2 Auroral shifts and magnetodisk variability*

347       Next we consider whether the observed Ganymede footprint and main auroral emission  
348 shifts display any dependence on the magnetospheric field configuration as indicated by the best  
349 fit magnetodisk parameter  $\mu_0 I_0$  calculated by Vogt et al. (2017). The best fit  $\mu_0 I_0$  values were  
350 calculated using Galileo magnetometer data during intervals when the spacecraft was located at  
351 radial distances between 10 and 30  $R_J$  in each orbit. Roughly half (68 of 143) of the 143 images  
352 used in this study overlapped with or occurred within 2 days of these intervals. Those images  
353 come from 10 of the 31 Galileo orbits (C10, E15, E16, E18, C21, C22, C23, I24, I27, and G29)  
354 which featured slightly smaller-than-average best fit  $\mu_0 I_0$  values. The 68 images with  
355 simultaneous/near-simultaneous current sheet measurements include 19 images with a clearly  
356 identified Ganymede footprint. The best fit  $\mu_0 I_0$  values at the times of our HST images range  
357 from 428 to 494 nT, with a mean of 463 nT. By comparison, the best fit  $\mu_0 I_0$  values from the full  
358 Galileo data set range from 406 to 572 nT, with a mean of 476 nT (see Vogt et al., 2017, table 1).

359       Figure 9 shows plots of the main emission shift, Ganymede footprint shift, and the  
360 difference between the Ganymede footprint shift and main emission shift as functions of the best  
361 fit  $\mu_0 I_0$  values corresponding to the dates of each image. In Figure 9a and in the middle panel of  
362 Figure 3 the error bars plotted for the Ganymede footprint shift indicate the possible range of  
363 shift values due to the 8 pixel uncertainty in the footprint latitude and longitude assumed by  
364 Bonfond et al. (2017). In Figure 9b and in the bottom panel of Figure 3 the error bars indicate the

365 standard deviation of the distance between the observed main emission points and the CML-  
366 specific reference contour.

367 By our definition a positive auroral shift means a shift poleward of the statistical main  
368 emission or satellite footprint reference contour, which would be consistent with a small current  
369 sheet current density  $\mu_0 I_0$  or a mostly dipole-like field geometry (see Figure 1), while a negative  
370 or equatorward shift would be consistent with a larger  $\mu_0 I_0$  and more radially stretched field  
371 configuration (see Figure 1). Therefore, we expect a negative correlation between the current  
372 sheet  $\mu_0 I_0$  fit and the two auroral shifts plotted in Figure 9a and Figure 9b. The main emission  
373 shift plotted in Figure 9a is very scattered but there is a very weak anti-correlative trend, with the  
374 smallest  $\mu_0 I_0$  values featuring only positive shifts. However, the Ganymede footprint shifts  
375 plotted in Figure 9b are nearly all positive and they appear to vary independently of the  $\mu_0 I_0$  fit  
376 values.

377 The difference between the Ganymede footprint shift and the main emission shift is  
378 plotted in Figure 9c. This shift difference is a useful quantity to consider because it provides  
379 information about whether the Ganymede footprint and main emission grow closer together or  
380 farther apart compared to the distance between their reference contours. We plot the shift  
381 difference rather than the distance between the Ganymede footprint and the main emission  
382 because the latter quantity depends on several factors, like the satellite longitude and CML, in  
383 addition to the current sheet  $\mu_0 I_0$  term, so identifying its  $\mu_0 I_0$  dependence from observations is  
384 not straightforward. The shift difference plotted in Figure 9c will be zero if both the Ganymede  
385 footprint and the main emission move latitudinally by the same distance and in the same  
386 direction. The shift difference will be positive if the Ganymede footprint and main emission get  
387 closer together (if the Ganymede footprint shifts more poleward than the main emission does, or

388 if the Ganymede footprint shifts less equatorward than the main emission does) and will be  
389 negative if the footprint and main emission get farther apart. We expect the distance between  
390 contours that map to two fixed positions in the magnetosphere (i.e. 15  $R_J$  and 30  $R_J$ ) to decrease  
391 with increasing radial field stretching or current sheet  $\mu_0 I_0$  term (see Figure 1 top right).  
392 Therefore, if the radial mapping of the main auroral emission is constant in time then we expect  
393 the shift difference plotted in Figure 9c to be positively correlated with  $\mu_0 I_0$ . However, as was  
394 the case for the main emission shift plotted in Figure 9a, the shift difference plotted in Figure 9c  
395 shows some scatter but overall shows a very weak anti-correlation with  $\mu_0 I_0$ , with most negative  
396 values occurring at large  $\mu_0 I_0$ .

397 Finally, time series of the Ganymede footprint and main auroral emission shifts are  
398 plotted in the bottom two panels of Figure 3 for comparison to the best fit  $\mu_0 I_0$  time series in the  
399 top panel. Galileo measurements of the best fit  $\mu_0 I_0$ , magnetospheric electron density, and Io  
400 dust emission rate, and ground-based observations of the Io plasma torus intensity all show a  
401 long-term decrease from roughly 1997 to 2000 (Krüger et al., 2003; Nozawa et al., 2004, 2005).  
402 Unfortunately, the HST observations are too sporadic during that interval, and too variable  
403 overall, to identify any corresponding long-term trend in the auroral shifts.

404

#### 405 *4.3 Main emission mapping: CML and temporal variability*

406 We now turn to the question of how the main emission's equatorial mapping changes in  
407 time. We begin by identifying the average main emission mapping then proceed to compare the  
408 observed CML dependence of the average main emission location identified in section 3 (Figure  
409 5) to the variability over a Jovian rotation period predicted from a mapping model. This analysis  
410 is useful to assess whether the observed CML dependence is indicative of a real spatial (CML)

411 variability or whether it reflects temporal changes or other biases. We then consider the observed  
412 main emission latitudinal shifts in the context of the measured current sheet current density  
413 changes and discuss implications for the magnetosphere-ionosphere coupling system.

414 For our mapping we primarily use the flux equivalence approach of Vogt et al. (2011),  
415 which is more reliable than tracing field lines from most global models in the middle and outer  
416 magnetosphere because it incorporates an empirical model of the magnetic field in those regions  
417 and accounts for local time asymmetries. This mapping approach is based on the assumption that  
418 the magnetic flux through a region in the ionosphere must equal the flux through the region to  
419 which it maps in the equatorial magnetosphere. The model uses a 2-D (radial distance and local  
420 time) empirical fit to magnetometer data to calculate the flux threading the equator and a model  
421 of Jupiter's internal magnetic field to calculate the flux through the ionosphere. Full details are  
422 available in Vogt et al. (2011). We note that the mapping results presented here use the Juno-era  
423 JRM09 magnetic field model (Connerney et al., 2018) as the internal field model in the flux  
424 mapping. The choice of internal field model can have a significant quantitative effect on the  
425 magnetosphere-ionosphere mapping of a specific point (Vogt et al., 2015), but we have  
426 confirmed that our choice of internal field model does not significantly change the qualitative  
427 findings presented here. Finally, we note that the mapping model depends on CML but does not  
428 include any other temporal variability (i.e. on time scales longer than one jovian day).

429 Figure 10 shows the main auroral emission mapping to the jovigraphic equator as a  
430 function of the mapped local time. The mapping shows some dependence on hemisphere and  
431 whether one employs the flux mapping (red and blue lines) or fieldline tracing (black lines)  
432 approach but overall, the main emission typically maps to  $\sim 20\text{-}40 R_J$ . The red lines show the  
433 average mapped location obtained by averaging the individual flux mapping results from each

434 HST image, and the blue lines show the flux mapping result of the statistical reference contour.  
435 If the main emission is linked to processes occurring in the equatorial magnetosphere, like  
436 corotation breakdown in the CEC theory, we would expect very close agreement between the  
437 northern (solid lines) and southern (dashed lines) radial distance mapping. There is a north-south  
438 difference in the mapping in Figure 10, but the mapping shows a systematic local time trend for  
439 both hemispheres. With the exception of the southern hemisphere reference contour flux  
440 mapping (blue dashed line), all mapping approaches suggest that the main emission maps to  
441 larger distances near dusk than near dawn by about 10-15  $R_J$ . Therefore, we suggest that the  
442 north-south mapping discrepancy could be due to systematic biases in the data used to create the  
443 northern or southern reference contours or could indicate the uncertainty in the mapping.

444         The Vogt et al. (2011) flux mapping model predicts that the ionospheric mapping of a  
445 fixed position in the equator will vary over the course of a jovian rotation period because of local  
446 time asymmetries in the magnetosphere. The model predicts that ionospheric contours that map  
447 to a fixed equatorial radial distance will be located more poleward where they map to local times  
448 near dusk than where they map to dawn local times, as we illustrate in supplemental figure S1.  
449 This point can also be seen in the middle panel of Figure 7, where the different colored mapped  
450  $50 R_J$  contours are shifted poleward near dusk and equatorward near dawn. Since the portion of  
451 the main emission that maps to a specific local time rotates with CML, magnetospheric local  
452 time asymmetries are manifested in auroral images as a CML-dependent latitudinal shift in the  
453 location of the main auroral emission.

454         We investigate the expected CML dependence in Figure 7, which compares the observed  
455 CML dependence of the main auroral emission to the CML dependence predicted using the Vogt  
456 et al. (2011) mapping model with JRM09 as the internal field model. Here we consider the

457 mapping to  $50 R_J$ , though this distance is at the upper end of the typical main emission radial  
458 distance mapping (Figure 10), because the CML dependence we observe in the main emission is  
459 larger than the predicted variability at  $30 R_J$ . This is probably because the main emission  
460 mapping varies with local time (Figure 10), which further amplifies the expected CML  
461 dependence since a position on the main emission would shift even more poleward when it is  
462 linked to dusk local times (where it maps to a larger radial distance) compared to when it is  
463 linked to dawn local times (where it maps to a smaller radial distance).

464         The middle row of Figure 7 shows the ionospheric contours mapping to  $50 R_J$  in the  
465 magnetosphere at different CMLs corresponding roughly to the average CML of the images  
466 included in each bin: in northern hemisphere those CMLs are  $120^\circ$  (purple),  $160^\circ$  (blue),  $210^\circ$   
467 (green), and  $270^\circ$  (red), and in the southern hemisphere they are  $30^\circ$  (purple),  $90^\circ$  (blue), and  
468  $330^\circ$  (red). The black contours in the middle panel of Figure 7 show the ionospheric mapping for  
469 CMLs  $190^\circ$  and  $50^\circ$  for the northern and southern hemisphere, respectively, which are roughly  
470 the average CML values for the set of northern and southern images used in this study. Finally,  
471 the bottom row of Figure 7 shows the magnetic latitudinal shift between each CML-specific  
472 statistical main emission contours (colored lines) and the average statistical main emission  
473 contour (black) calculated from all images used in this study. We define the shift as positive if  
474 the CML-specific statistical main emission contour is poleward of the average statistical main  
475 emission contour and negative if it is equatorward. The solid lines show the observed latitudinal  
476 shift, or the magnetic latitude difference between the colored and black contours from the top  
477 panel of Figure 7, and the dashed lines show the magnetic latitude difference between the  
478 modeled colored and black contours from the middle panel of Figure 7.

479 By comparing the observed (solid) and predicted (dashed) latitudinal shifts in the bottom  
480 row of Figure 7 we see that the overall CML dependence observed in the main auroral emission  
481 is generally consistent with the CML dependence predicted by the ionospheric mapping from 50  
482  $R_J$ . For example, both CML 240°-290° in the north and CML 290°-360° in the south (red lines)  
483 feature a large poleward (positive) shift at large longitudes in both the observations and mapping  
484 predictions. The observed shifts in the other CML bins do not match the mapping predictions as  
485 closely but do generally match the direction of the modeled shift (i.e. poleward or equatorward)  
486 and the observed and mapped contours from the various CML bins generally appear in the same  
487 order from most poleward to most equatorward. Overall, we find that the observed and modeled  
488 CML dependence are broadly consistent with each other. Since the auroral mapping model has  
489 no temporal dependence this confirms that the observed main emission CML dependence is a  
490 real spatial, not temporal, variation that likely results from local time asymmetries in both the  
491 magnetosphere and the main emission equatorial mapping.

492 Finally, we show in Figure 11 the expected variability in the main emission position  
493 resulting from changes in the current sheet current density. We represent the main emission  
494 position by tracing model field lines from 30  $R_J$  in the jovigraphic equator and we assess the  
495 expected variability by altering the  $\mu_0 I_0$  parameter in the Connerney, Acuña, and Ness (1981)  
496 current sheet model (“CAN1981”) or the similar Juno-era current sheet model from Connerney  
497 et al. (2020) (“CON2020”). Both CAN1981 and CON2020 represent the perturbation magnetic  
498 field as that produced by an axisymmetric annular disk of azimuthal current with adjustable  
499 parameters including the inner edge  $R_o$ , outer edge  $R_l$ , half-thickness  $D$ , and current density  $I_0$ .  
500 (The CON2020 model additionally included the effects of the radial current which produces the  
501 azimuthal magnetic field that sweeps the field back out of the meridian plane.) The blue, green,

502 and red colored contours show the traced 30  $R_J$  mapping calculated using varying  $\mu_0 I_0$ ,  
503 representing low, average, and high current sheet current density, respectively, in the CAN1981  
504 and CON2020 current sheet models. We implemented the CAN1981 model using the Voyager-  
505 era fits for  $R_0$  (5  $R_J$ ),  $R_I$  (50  $R_J$ ), and  $D$  (2.5  $R_J$ ), and took  $\mu_0 I_0 = 400, 480, \text{ and } 560$  nT, roughly  
506 covering the range of Galileo-era fits (406 to 572 nT with a mean of 476 nT) from Vogt et al.  
507 (2017). We implemented the CON2020 model using the Juno-era fits for  $R_0$  (7.8  $R_J$ ),  $R_I$  (51.4  
508  $R_J$ ), and  $D$  (3.6  $R_J$ ), with the mean value of  $\mu_0 I_\rho / 2\pi = 16.7$  nT, and took  $\mu_0 I_0 = 240, 280, \text{ and}$   
509  $320$  nT, roughly covering the range of Juno-era fits (248.4 to 312.2 nT with a mean of 279.2 nT)  
510 as reported by Connerney et al. (2020).

511 We can compare the variability of the colored contours – representing low, average, and  
512 high current sheet current density – to the variability in the main emission position as indicated  
513 by the small shaded gray bins of  $2^\circ$  magnetic longitude by  $0.1^\circ$  magnetic latitude. We have  
514 shaded in all bins for which the main emission was located in that area in at least two of the  
515 images used in this study, which eliminates some of the extreme outliers (see e.g. dark purple  
516 high-latitude bins in the distribution of the main emission locations shown in Figure 5). The  
517 different panels of Figure 11 show 30  $R_J$  fieldline tracing results obtained using CAN1981 plus  
518 the internal field of the Grodent Anomaly Model or GAM (Grodent et al., 2008b) in the north  
519 and VIP4 (Connerney et al., 1981) in the south and CAN2020 plus JRM09 (Connerney et al.,  
520 2018) in both the north and south. There is considerable variation in how well the mapped 30  $R_J$   
521 contours of the different field models/options match the main emission locations. However, we  
522 can see that the predicted variability in the main auroral emission position as indicated by the  
523 spacing of the colored contours is roughly consistent with the observed variability as indicated  
524 by the spread of the gray shaded bins.

525

#### 526 *4.4 Discussion and future work*

527         The results described above include some unexpected and sometimes conflicting  
528 conclusions about the latitudinal variability of the main auroral emission, its relationship to  
529 variability in the Ganymede footprint position, and the influence of changes in the current sheet  
530 current density. In particular, the absence of a clear relationship between the Ganymede footprint  
531 shift and the concurrent  $\mu_0 I_0$  fit by Galileo is puzzling. The most likely explanation is that errors  
532 in the planetary limb fitting procedure led to incorrect footprint locations and the derived  
533 footprint shifts. However, it is also important to remember that the limited HST data set  
534 considered here, particularly when considering the subset of images that contain the Ganymede  
535 footprint, does not encompass times of the most extreme  $\mu_0 I_0$  values. We note, for example, that  
536 most of the Ganymede footprint shifts measured here are positive, indicating a position poleward  
537 of the reference footpath, which would be expected for a weaker than normal current sheet  
538 stretching. This is consistent with the fact that the Galileo  $\mu_0 I_0$  fits at the time of the HST images  
539 ranged from  $\sim 430$ - $500$  nT, while the Galileo  $\mu_0 I_0$  fits from all orbits ranged from  $406$  to  $572$  nT.  
540 Finally, we note that the typical Ganymede footprint shift observed here,  $\sim 0.5^\circ$  poleward, is  
541 roughly consistent with the total difference,  $\sim 1.5^\circ$ , expected between the strongest and weakest  
542 current sheet fits to all Galileo data (top right of Figure 1). In the future, expanding our analysis  
543 to include Juno  $\mu_0 I_0$  fits (Connerney et al., 2020) and Juno-HST concurrent images could help  
544 fill out the range of  $\mu_0 I_0$  values under consideration and evince the expected relationship  
545 between the Ganymede footprint shift and  $\mu_0 I_0$ .

546         As a final explanation for the absent expected correlation between the Ganymede  
547 footprint shift and the Galileo  $\mu_0 I_0$  fit, we note that it is possible that the time or spatial scales of

548 Jupiter’s current sheet variability might be inconsistent with the type of snapshot comparison to  
549 HST images that we have attempted here. For example, it is possible that the magnetic field  
550 configuration at the time of some HST images was influenced by a transient process like a  
551 magnetospheric injection (e.g. Mauk et al., 1999), tail reconfiguration (e.g. Louarn et al., 2014),  
552 or solar wind compression (e.g. Vogt et al., 2019) that occurred on a time scale that was short  
553 (~hours to tens of hours) compared to the ~5-10 day intervals over which the  $\mu_0 I_0$  fits were  
554 calculated. Such a transient process could produce a brief Ganymede footprint shift that is  
555 inconsistent with the  $\mu_0 I_0$  fit. There were some Galileo orbits for which the inbound and  
556 outbound  $\mu_0 I_0$  fits of each orbit varied significantly, as shown by the handful of points with large  
557 error bars in the top panel of Figure 3, but the  $\mu_0 I_0$  fit values were generally stable on the ~5-10  
558 day timescale. The  $\mu_0 I_0$  values plotted in Figure 9 are the average values for each orbit but  
559 similar plots made using the  $\mu_0 I_0$  fits from separate inbound or outbound orbit segments, shown  
560 in Figure S2, also do not show the expected relationship between the footprint shift and  $\mu_0 I_0$ . It  
561 is also possible that any magnetic field stretching or compression observed by Galileo is limited  
562 in local time and does not necessarily extend to Ganymede’s location, which would explain why  
563 the footprint shift did not display the expected dependence on  $\mu_0 I_0$ . As shown in the right side of  
564 Figure 2, Galileo was generally located at dusk and nightside local times (~16:00 and later) when  
565 it was located between 10 and 30  $R_J$ , the radial distance range over which Vogt et al. (2017)  
566 calculated the  $\mu_0 I_0$  fits. By comparison, almost all of the Ganymede footprints we analyzed in  
567 this study map to earlier local times, roughly 08:00-12:00. However, we note that the Galileo  
568  $\mu_0 I_0$  fits were generally similar for both the inbound and outbound portions of an orbit, which  
569 could be at significantly different local times, so we feel this explanation is somewhat unlikely.

570           The analysis we have undertaken here naturally leads to several interesting topics for  
571 future work. Here we have considered only auroral position and not other auroral properties like  
572 brightness or the width of the main emission, which (Nichols et al., 2009), and a future study  
573 could assess whether these properties are linked to changes observed in the magnetodisk or  
574 variability in the satellite footprint locations. Computational magnetosphere-ionosphere coupling  
575 models like those applied in Nichols (2011) and Nichols et al. (2015) can be used to examine  
576 how variability in the corotation enforcement current system can produce the auroral shifts we  
577 have studied here, and model results could be compared to Galileo data. Finally, we hope in the  
578 future to more thoroughly analyze the Galileo magnetometer data and additional Galileo datasets  
579 like the hectometric auroral radio emissions and energetic particle detector (EPD) measurements  
580 for context about the state of Jupiter’s magnetosphere at the time of each HST image. For  
581 example, Galileo data can help infer whether, at the time of each HST image, the magnetosphere  
582 was experiencing a solar wind compression or other dynamic behavior such as a quasi-periodic  
583 interval of magnetic loading/unloading (e.g. Kronberg et al., 2005, 2007; Louarn et al., 2014;  
584 Yao et al., 2019), and the measured variability in the magnetic field and plasma properties  
585 provide a valuable constraint to M-I coupling models.

586

## 587 **5. Summary**

588           We have identified the position of the main auroral emission in all HST images that  
589 overlapped with the Galileo mission (1996-2003). We have quantified the variability in the main  
590 emission position and compared it to concurrent shifts in the position of the Ganymede footprint  
591 and to changes in the current sheet current density  $\mu_0 I_0$  fit to concurrent Galileo data. We expect  
592 that the position of the satellite footprints will depend on the  $\mu_0 I_0$  term, which provides a

593 measure of how radially stretched the magnetic field is, because the satellites are located at a  
594 fixed position in the magnetosphere and any motion in their auroral footprints should be linked  
595 to a change in the magnetic field configuration. By comparison, past observations have shown  
596 that the main auroral emission may shift independently (in magnitude and direction) of the  
597 satellite footprints, which would suggest that the variability can be driven by factors in the  
598 corotation enforcement current system or any other mechanism responsible for the main  
599 emissions that do not influence the magnetic field geometry.

600 We compared the magnitude and direction of latitudinal shifts in the main auroral  
601 emission and Ganymede footprint and found that the two auroral features generally moved  
602 together (i.e. both shifted poleward or both shifted equatorward with respect to a reference  
603 contour). However, we also found that the position (with respect to a reference contour) of both  
604 the main auroral emission and the Ganymede footprint are only weakly linked to the changes in  
605 the concurrent best fit  $\mu_0 I_0$ . The lack of the expected clear relationship between the Ganymede  
606 footprint behavior and the current sheet current density is puzzling and may reflect the  
607 uncertainty in the planetary limb fitting during the STIS image processing. Additionally, we  
608 found that there can be significant differences in the measured main emission position among  
609 images from the same day, even after accounting for the expected variability with CML / over a  
610 Jovian day, which is probably also indicative of the measurement uncertainties.

611 As part of our analysis we derived a northern and southern statistical main emission  
612 reference contours using all images in the north and south hemispheres, respectively, and also  
613 derived statistical reference contours using only images from specific CML ranges. We found  
614 that the main emission position shifts by  $\sim 1^\circ$ - $2^\circ$  over the course of one Jovian rotation and that  
615 the observed CML dependence is consistent with the mapping model predictions that account for

616 local time asymmetries in Jupiter's magnetosphere. Additionally, we mapped our derived  
617 statistical main emission reference contour to the magnetosphere using both a flux equivalence  
618 and field line tracing technique and found that the main emission typically maps to  $\sim 20\text{-}40 R_J$  in  
619 the equator and at larger distances near dusk than near dawn.

620 In summary, we have quantified the temporal and spatial (CML and local time)  
621 variability of the main auroral emission and Ganymede footprint during the Galileo era. We do  
622 not find a strong link between the auroral shifts and the current sheet current density fit to  
623 Galileo data but we expect that future studies will provide more insight into the drivers of the  
624 observed auroral variability, both by decreasing the uncertainty in the auroral position and by  
625 expanding our analysis to other Galileo and Juno datasets.

626

## 627 **Acknowledgments**

628 This work is based on observations with the NASA/ESA Hubble Space Telescope obtained from  
629 the Data Archive at the Space Telescope Science Institute  
630 (<https://archive.stsci.edu/hst/search.php>), which is operated by the Association of Universities for  
631 Research in Astronomy, Incorporated, under NASA contract NAS5-26555. Support for this work  
632 was provided through grant HST-AR-14576.001-A from the STScI under NASA contract NAS5  
633 26555. M.F.V. was supported in part by NASA Grant 80NSSC17K0777. B.B. is a FRS-FNRS  
634 research associate.

635

## 636 **References**

637

638 Bonfond, B., D. Grodent, J.-C. Gérard, T. Stallard, J. T. Clarke, M. Yoneda, A. Radioti, and J.  
639 Gustin (2012), Auroral evidence of Io's control over the magnetosphere of Jupiter, *Geophys. Res.*  
640 *Lett.*, 39, L01105, doi:10.1029/2011GL050253.

641

642 Bonfond, B., Saur, J., Grodent, D., Badman, S. V., Bisikalo, D., Shematovich, V., Gérard, J.-C.,  
643 and Radioti, A. (2017), The tails of the satellite auroral footprints at Jupiter, *J. Geophys. Res.*  
644 *Space Physics*, 122, 7985– 7996, doi:10.1002/2017JA024370.

645

646 Bonfond, B., Yao, Z., & Grodent, D. (2020). Six pieces of evidence against the corotation  
647 enforcement theory to explain the main aurora at Jupiter. *Journal of Geophysical Research:*  
648 *Space Physics*, 125, e2020JA028152. <https://doi.org/10.1029/2020JA028152>

649

650 Caldwell, J., B. Turgeon, and X.-M. Hua (1992), Hubble Space Telescope Imaging of the North  
651 Polar Aurora on Jupiter, *Science*, 257, 1512-1515.

652

653 Clarke, J. T., J. Ajello, G. Ballester, L. B. Jaffel, J. Connerney, J.-C. Gérard, G. R. Gladstone, D.  
654 Grodent, W. Pryor, J. Trauger, and J. H. Waite Jr. (2002), Ultraviolet emissions from the  
655 magnetic footprints of Io, Ganymede and Europa on Jupiter, *Nature*, 415, 997.

656

657 Clarke, J. T., J. Nichols, J.-C. Gérard, D. Grodent, K. C. Hansen, W. Kurth, G. R. Gladstone, J.  
658 Duval, S. Wannawichian, E. Bunce, S. W. H. Cowley, F. Crary, M. Dougherty, L. Lamy, D.  
659 Mitchell, W. Pryor, K. Retherford, T. Stallard, B. Zieger, P. Zarka, and B. Cecconi (2009),  
660 Response of Jupiter's and Saturn's auroral activity to the solar wind, *J. Geophys. Res.*, 114,

661 A05210, doi:10.1029/2008JA013694.

662

663 Connerney, J., M. Acuña, and N. Ness (1981), Modeling the Jovian Current Sheet and Inner  
664 Magnetosphere, *J. Geophys. Res.*, *86*(A10), 8370-8384.

665

666 Connerney, J. E. P., M. H. Acuña, N. F. Ness, and T. Satoh, (1998), New models of Jupiter's  
667 magnetic field constrained by the Io flux tube footprint, *J. Geophys. Res.*, *103*, 11929-11939.

668

669 Connerney, J. E. P., Kotsiaros, S., Oliverson, R. J., Espley, J. R., Joergensen, J. L., Joergensen, P.  
670 S., et al. (2018). A new model of Jupiter's magnetic field from Juno's first nine orbits.  
671 *Geophysical Research Letters*, *45*. <https://doi.org/10.1002/2018GL077312>

672

673 Connerney, J. E. P., Timmins, S., Hecceg, M., & Joergensen, J. L. (2020). A Jovian magnetodisc  
674 model for the Juno era. *Journal of Geophysical Research: Space Physics*, *125*, e2020JA028138.  
675 <https://doi.org/10.1029/2020JA028138>

676

677 Cowley, S. W. H., and E. J. Bunce (2001), Origin of the main auroral oval in Jupiter's coupled  
678 magnetosphere-ionosphere system, *Plan. Space Sci.*, *49*, 1067-1088.

679

680 Elliott, S. S., Gurnett, D. A., Kurth, W. S., Clark, G., Mauk, B. H., Bolton, S. J., ... Levin, S. M.  
681 (2018). Pitch angle scattering of upgoing electron beams in Jupiter's polar regions by whistler  
682 mode waves. *Geophysical Research Letters*, *45*, 1246– 1252.  
683 <https://doi.org/10.1002/2017GL076878>

684

685 Gershman, D. J., Connerney, J. E. P., Kotsiaros, S., DiBraccio, G. A., Martos, Y. M., F.-Viñas,  
686 A., et al. (2019). Alfvénic fluctuations associated with Jupiter's auroral emissions. *Geophysical*  
687 *Research Letters*, *46*, 7157–7165. <https://doi.org/10.1029/2019GL082951>

688

689 Grodent, D., J. T. Clarke, J. Kim, J. H. Waite, and S. W. H. Cowley (2003), Jupiter's main  
690 auroral oval observed with HST-STIS, *J. Geophys. Res.*, *108*, 1389, doi:10.1029/2003JA009921,  
691 A11.

692

693 Grodent, D., J.-C. Gérard, A. Radioti, B. Bonfond, and A. Saglam (2008a), Jupiter's changing  
694 auroral location, *J. Geophys. Res.*, *113*, A01206, doi:10.1029/2007JA012601.

695

696 Grodent, D., B. Bonfond, J.-C. Gérard, A. Radioti, J. Gustin, J. T. Clarke, J. Nichols, and J. E. P.  
697 Connerney (2008b), Auroral evidence of a localized magnetic anomaly in Jupiter's northern  
698 hemisphere, *J. Geophys. Res.*, *113*, A09201, doi:10.1029/2008JA013185.

699

700 Hill, T. W. (2001), The Jovian auroral oval, *J. Geophys. Res.*, *106*, 8101-8107.

701

702 Joy, S. P., M. G. Kivelson, R. J. Walker, K. K. Khurana, C. T. Russell, and T. Ogino (2002),  
703 Probabilistic models of the Jovian magnetopause and bow shock locations, *J. Geophys. Res.*,  
704 *107*, 1309, doi: 10.1029/2001JA009146.

705

706 Kronberg, E. A., J. Woch, N. Krupp, A. Lagg, K. K. Khurana, and K.-H. Glassmeier (2005),  
707 Mass release at Jupiter: Substorm-like processes in the Jovian magnetotail, *J. Geophys. Res.*,  
708 *110*, A03211, doi:10.1029/2004JA010777.

709

710 Kronberg, E. A., K.-H. Glassmeier, J. Woch, N. Krupp, A. Lagg, and M.K. Dougherty (2007), A  
711 possible intrinsic mechanism for the quasi-periodic dynamics of the Jovian magnetosphere, *J.*  
712 *Geophys. Res.*, *112*, A05203.

713

714 Krüger, H., P. Geissler, M. Horányi, A. L. Graps, S. Kempf, R. Srama, G. Moragas-  
715 Klostermeyer, R. Moissl, T. V. Johnson, and E. Grün (2003), Jovian dust streams: A monitor of  
716 Io's volcanic plume activity, *Geophys. Res. Lett.*, *30*, 2101, doi:10.1029/2003GL017827, 21.

717

718 Louarn, P., C. P. Paranicas, and W. S. Kurth (2014), Global magnetodisk disturbances and energetic  
719 particle injections at Jupiter, *J. Geophys. Res. Space Physics*, *119*, 4495–4511,  
720 doi:10.1002/2014JA019846.

721

722 Lysak, R. L., & Song, Y. (2020). Field line resonances in Jupiter's magnetosphere. *Geophysical*  
723 *Research Letters*, *47*, e2020GL089473. <https://doi.org/10.1029/2020GL089473>

724

725 Mauk, B. H., D. J. Williams, R. W. McEntire, K. K. Khurana, and J. G. Roederer (1999), Storm-  
726 like dynamics of Jupiter's inner magnetosphere, *J. Geophys. Res.*, *104*, 22,759.

727

728 Nichols, J. D. (2011), Magnetosphere-ionosphere coupling in Jupiter's middle magnetosphere:  
729 Computations including a self-consistent current sheet magnetic field model, *J. Geophys. Res.*,  
730 *116*, A10232, doi:[10.1029/2011JA016922](https://doi.org/10.1029/2011JA016922).  
731

732 Nichols, J. D. and S. W. H. Cowley (2004), Magnetosphere-ionosphere coupling currents in  
733 Jupiter's middle magnetosphere: effect of precipitation-induced enhancement of the ionospheric  
734 Pedersen conductivity, *Ann. Geophys.*, *22*, 1799-1827, doi:[10.5194/angeo-22-1799-2004](https://doi.org/10.5194/angeo-22-1799-2004).  
735

736 Nichols, J. D., J. T. Clarke, J. C. Gérard, and D. Grodent (2009), Observations of Jovian polar  
737 auroral filaments, *Geophys. Res. Lett.*, *36*, L08101, doi:[10.1029/2009GL037578](https://doi.org/10.1029/2009GL037578).  
738

739 Nichols, J. D., N. Achilleos, and S. W. H. Cowley (2015), A model of force balance in Jupiter's  
740 magnetodisc including hot plasma pressure anisotropy, *J. Geophys. Res. Space Physics*, *120*,  
741 10,185–10,206, doi:[10.1002/2015JA021807](https://doi.org/10.1002/2015JA021807).  
742

743 Nichols, J. D., Allegrini, F., Bagenal, F., Bunce, E. J., Cowley, S. W. H., Ebert, R. W., et al.  
744 (2020). An enhancement of Jupiter's main auroral emission and magnetospheric currents.  
745 *Journal of Geophysical Research: Space Physics*, *125*, e2020JA027904.  
746 <https://doi.org/10.1029/2020JA027904>  
747

748 Nozawa, H., H. Misawa, S. Takahashi, A. Morioka, S. Okano, and R. Sood (2004), Long-term  
749 variability of [SII] emissions from the Io plasma torus between 1997 and 2000, *J. Geophys. Res.*,  
750 *109*, A07209, doi:[10.1029/2003JA010241](https://doi.org/10.1029/2003JA010241).

751

752 Nozawa, H., H. Misawa, S. Takahashi, A. Morioka, S. Okano, and R. Sood (2005), Relationship  
753 between the Jovian magnetospheric plasma density and Io torus emission, *Geophys. Res. Lett.*,  
754 32, L11101, doi:10.1029/2005GL022759.

755

756 Pan, D-X., Yao, Z-H., Manners, H., Dunn, W., Bonfond, B., Grodent, D., et al. (2021). Ultralow-  
757 frequency waves in driving Jovian aurorae revealed by observations from HST and Juno.  
758 *Geophysical Research Letters*, 48, e2020GL091579. <https://doi.org/10.1029/2020GL091579>

759

760 Radioti, A., J.-C. Gérard, D. Grodent, B. Bonfond, N. Krupp, and J. Woch (2008), Discontinuity  
761 in Jupiter's main auroral oval, *J. Geophys. Res.*, 113, A01215, doi:10.1029/2007JA012610.

762

763 Saur, J., Janser, S., Schreiner, A., Clark, G., Mauk, B. H., Kollmann, P., Kollmann, P., Ebert, R.  
764 W., Allegrini, F., Szalay, J. R., & Kotsiaros, S. (2018). Wave-particle interaction of Alfvén  
765 waves in Jupiter's magnetosphere: Auroral and magnetospheric particle acceleration. *Journal of*  
766 *Geophysical Research: Space Physics*, 123, 9560– 9573. <https://doi.org/10.1029/2018JA025948>

767

768 Thomas, N., F. Bagenal, T. W. Hill, and J. K. Wilson (2004), in *Jupiter: the Planet, Satellites,*  
769 *and Magnetosphere*, edited by F. Bagenal et al., Cambridge Univ. Press, New York.

770

771 Vogt, M. F., M. G. Kivelson, K. K. Khurana, R. J. Walker, B. Bonfond, D. Grodent, and A.  
772 Radioti (2011), Improved mapping of Jupiter's auroral features to magnetospheric sources, *J.*  
773 *Geophys. Res.*, 116, A03220, doi:10.1029/2010JA016148.

774

775 Vogt, M. F., E. J. Bunce, M. G. Kivelson, K. K. Khurana, R. J. Walker, A. Radioti, B. Bonfond,  
776 and D. Grodent (2015), Magnetosphere-ionosphere mapping at Jupiter: Quantifying the effects  
777 of using different internal field models, *J. Geophys. Res. Space Physics*, *120*, 2584–2599,  
778 doi:10.1002/2014JA020729.

779

780 Vogt, M. F., E. J. Bunce, J. D. Nichols, J. T. Clarke, and W. S. Kurth (2017), Long-term  
781 variability of Jupiter’s magnetodisk and implications for the aurora, *Journal of Geophysical*  
782 *Research: Space Physics*, *122*, 12,090–12,110, doi:10.1002/2017JA024066.

783

784 Vogt, M. F., Gyalay, S., Kronberg, E. A., Bunce, E. J., Kurth, W. S., Zieger, B., & Tao, C.  
785 (2019). Solar wind interaction with Jupiter's magnetosphere: A statistical study of Galileo in situ  
786 data and modeled upstream solar wind conditions. *Journal of Geophysical Research: Space*  
787 *Physics*, *124*, 10170–10199. <https://doi.org/10.1029/2019JA026950>

788

789 Yao, Z. H., Grodent, D., Kurth, W. S., Clark, G., Mauk, B. H., Kimura, T., Bonfond, B., Ye, S.  
790 Y., Lui, A. T., Radioti, A., & Palmaerts, B. (2019). On the relation between Jovian aurorae and  
791 the loading/unloading of the magnetic flux: Simultaneous measurements from Juno, HST and  
792 Hisaki. *Geophysical Research Letters*, *46*(21), 11,632–11,641.

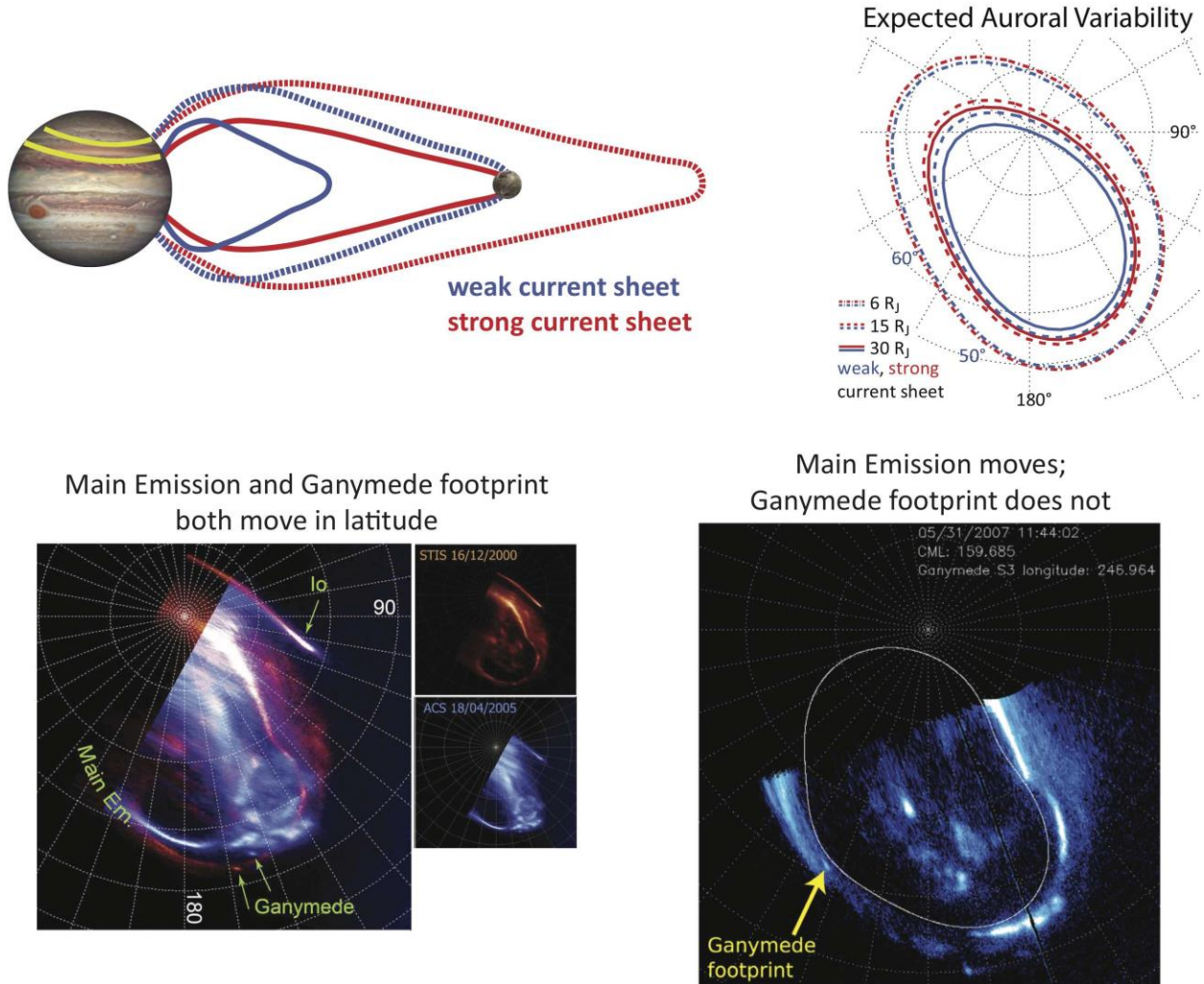
793 <https://doi.org/10.1029/2019GL084201>

794

795 Yao, Z., W. R. Dunn, E. E. Woodfield, G. Clark, B. H. Mauk, R. W. Ebert, D. Grodent, B.  
796 Bonfond, D. Pan, I. J. Rae, B. Ni, R. Guo, G. Branduardi-Raymont, A. D. Wibisono, R.

797 Rodriguez, S. Kotsiaros, J.-U. Ness, F. Allegrini, W. S. Kurth, G. R. Gladstone, R. Kraft, A. H.  
798 Sulaiman, H. Manners, R. T. Desai, and S. J. Bolton, Revealing the source of Jupiter's x-ray  
799 auroral flares, *Science Advances*, 10.1126/sciadv.abf0851, 7, 28, (eabf0851), (2021).  
800

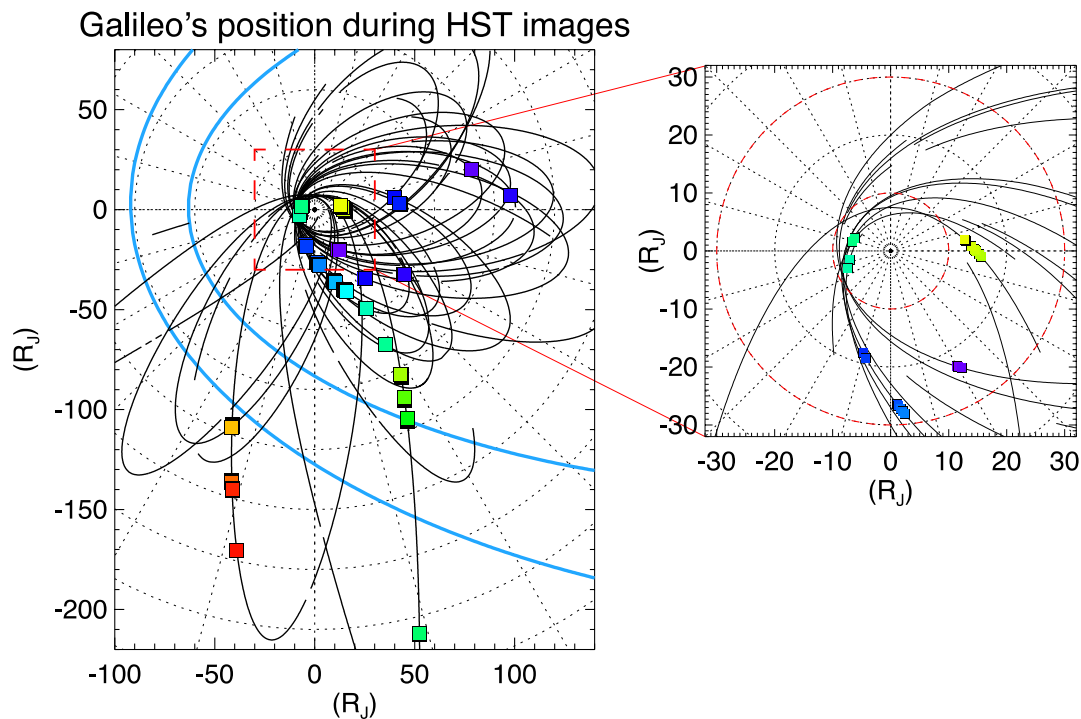
801



802

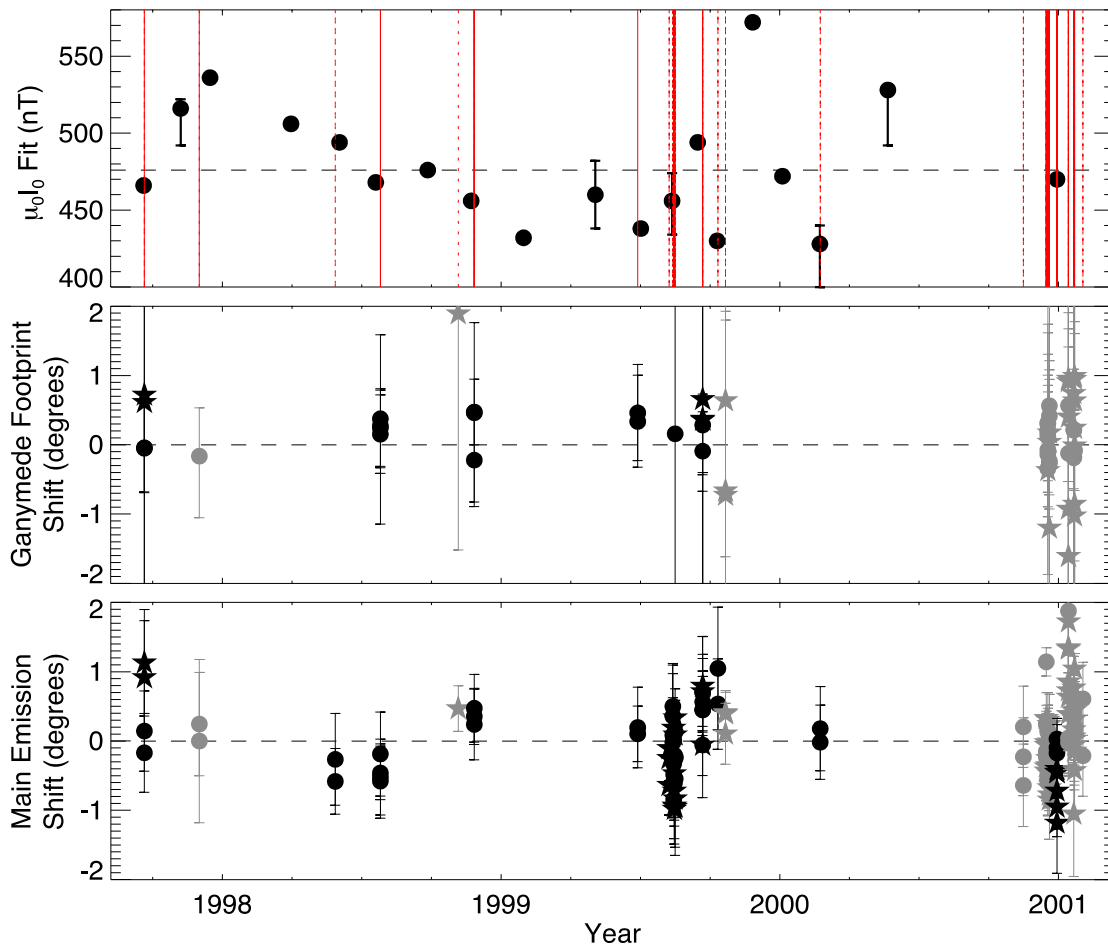
803 **Figure 1.** (Top left) Illustration showing how a change in the configuration of magnetic field  
804 lines in Jupiter's magnetosphere can lead to a latitudinal shift in auroral features like the main  
805 emission or a satellite footprint (not to scale). The blue (red) field lines show the field  
806 configuration for a weak (strong) current sheet. (Top right) Results of tracing model field lines to  
807 the northern ionosphere from 6 R<sub>J</sub> (dash-dot), 15 R<sub>J</sub> (dashed), and 30 R<sub>J</sub> (solid) in the jovigraphic  
808 equator assuming a weak (blue) or strong (red) current sheet consistent with the measured  
809 current sheet variability observed by Galileo. Modified from Figure 8 of Vogt et al. (2017).  
810 (Bottom left) Two HST polar auroral images from 2000 (red) and 2005 (blue) are overlaid,

811 showing how the Ganymede footprint and main auroral emission can shift latitudinally by  
 812 several degrees. Reproduced from Grodent et al. (2008a). (Bottom right) HST polar image of  
 813 Jupiter's aurora from Bonfond et al. (2012) in which the main auroral emission is so expanded  
 814 that it is located equatorward of the Ganymede footprint. The white line shows the Bonfond et al.  
 815 (2012) reference main emission.  
 816



817  
 818 **Figure 2.** (Left) Black lines show the orbital path of the Galileo spacecraft projected onto the  
 819 equatorial plane, with the sun to the left. Lines are drawn only at times with available magnetic  
 820 field measurements. Colored boxes show Galileo's position at the times of the 143 HST images  
 821 used in this study, with the exception of the two HST images from 28 May 1998 (DOY 148),  
 822 when no magnetometer data are available. Light blue lines show the positions of the expanded  
 823 and compressed Joy et al. (2002) magnetopause. (Right) Galileo's orbital path projected onto the  
 824 equatorial plane (black lines) along with its position at the times of HST images (colored

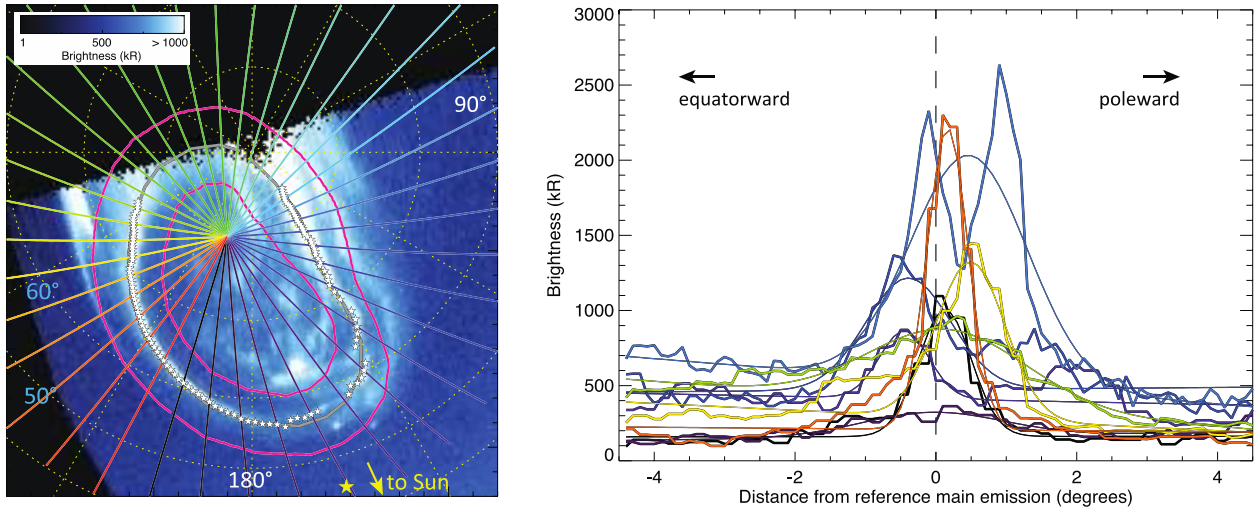
825 squares) in the inner and middle magnetosphere. Galileo's trajectory is shown only for the 10  
 826 orbits for which HST images overlap or nearly overlap with intervals when the current sheet best  
 827 fit  $\mu_0 I_0$  was calculated (when the spacecraft was located between 10 and 30  $R_J$  – see the red  
 828 dashed circles).  
 829



830  
 831 **Figure 3.** Time series of the current sheet current density,  $\mu_0 I_0$ , and auroral shifts during the  
 832 Galileo era. (top) Best fit  $\mu_0 I_0$  calculated using Galileo data as a function of time. Error bars  
 833 show the variability obtained by fitting the inbound and outbound portions of each Galileo orbit  
 834 separately (see text). Red lines show times of the HST images used in this study with (solid) and

835 without (dashed) a visible Ganymede footprint. The dashed horizontal line at 476 nT indicates  
 836 the average  $\mu_0 I_0$  fit from all Galileo orbits. (middle) Ganymede footprint shift (see text) as a  
 837 function of time. In this and the next panel data from northern hemisphere images are plotted as  
 838 circles and data from southern hemisphere images are plotted as star symbols; gray symbols  
 839 indicate data from auroral images with no corresponding  $\mu_0 I_0$  fit. Both the Ganymede footprint  
 840 and main emission shifts are defined as positive if the relevant auroral feature is poleward of the  
 841 reference contour/footpath and negative if it is equatorward. Error bars indicate the uncertainty in  
 842 the Ganymede footprint position reported by Bonfond et al. (2017) (see text). (bottom) Mean  
 843 main auroral emission shift in each image, corrected for CML dependence (see text), as a  
 844 function of time. Error bars indicate the standard deviation of the main emission shift.

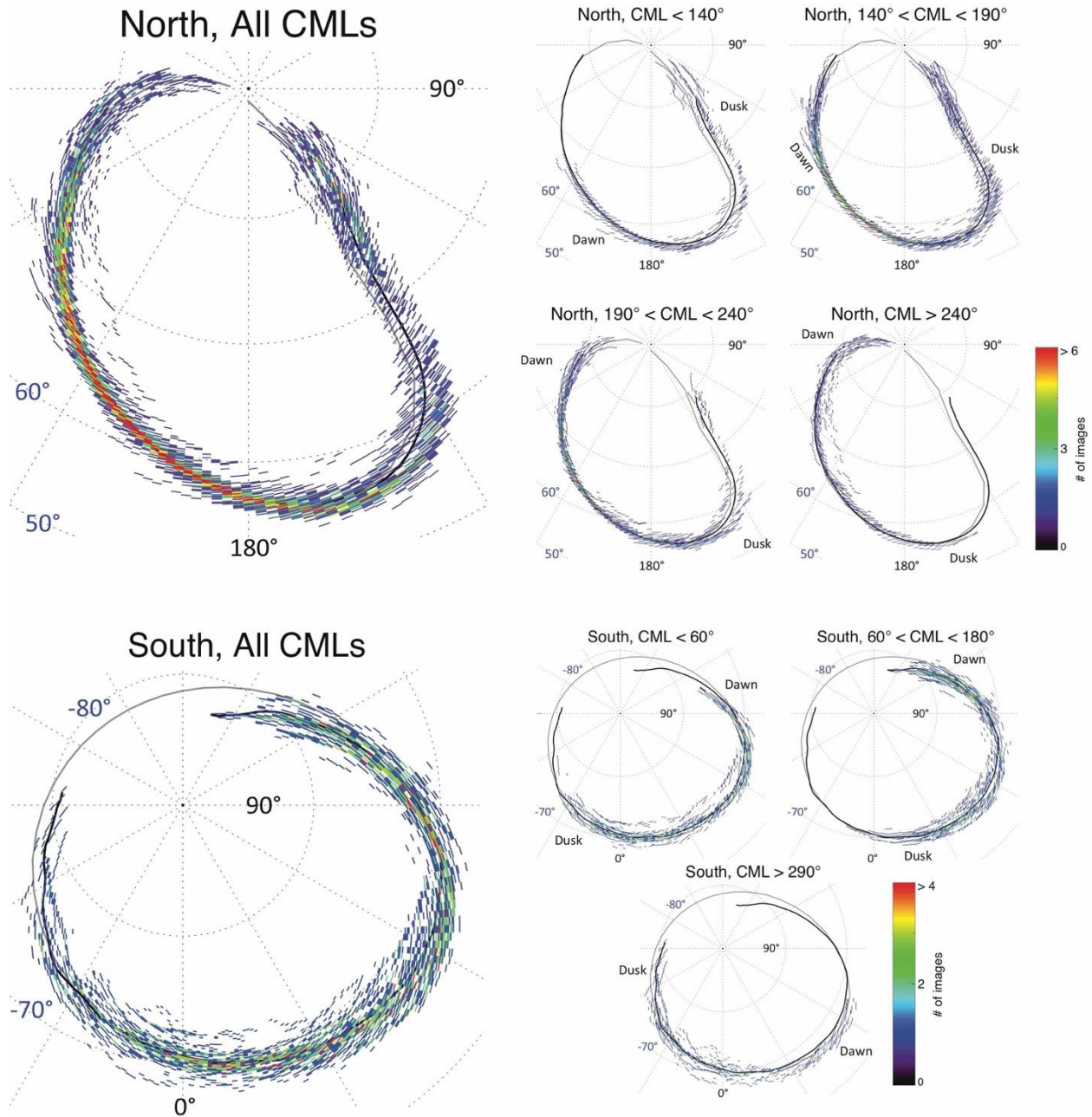
845



846

847 **Figure 4.** (left) Polar projection of an HST image taken on 25 November 1998 with CML 164.2°  
 848 (yellow star). Colored lines radiating outward from the magnetic pole show the magnetic  
 849 longitude “slices” along which we fit the auroral brightness with a Gaussian in the region  
 850 between the two pink contours. The gray line shows the reference main emission contour of  
 851 Nichols et al. (2009). White stars show the identified main emission locations for this image,

852 with a spacing of  $2^\circ$  magnetic longitude. System III left-handed longitude is noted in white text  
853 and latitude is noted in blue. (b) Auroral brightness (thick lines) and Gaussian fits (thin lines)  
854 along selected magnetic longitude “slices” from the left panel of Figure 4, plotted as a function  
855 of distance from the Nichols et al. (2009) reference contour in degrees of magnetic latitude. Each  
856 brightness profile has been plotted in the same color of the corresponding magnetic longitude  
857 slice.  
858



859

860

861

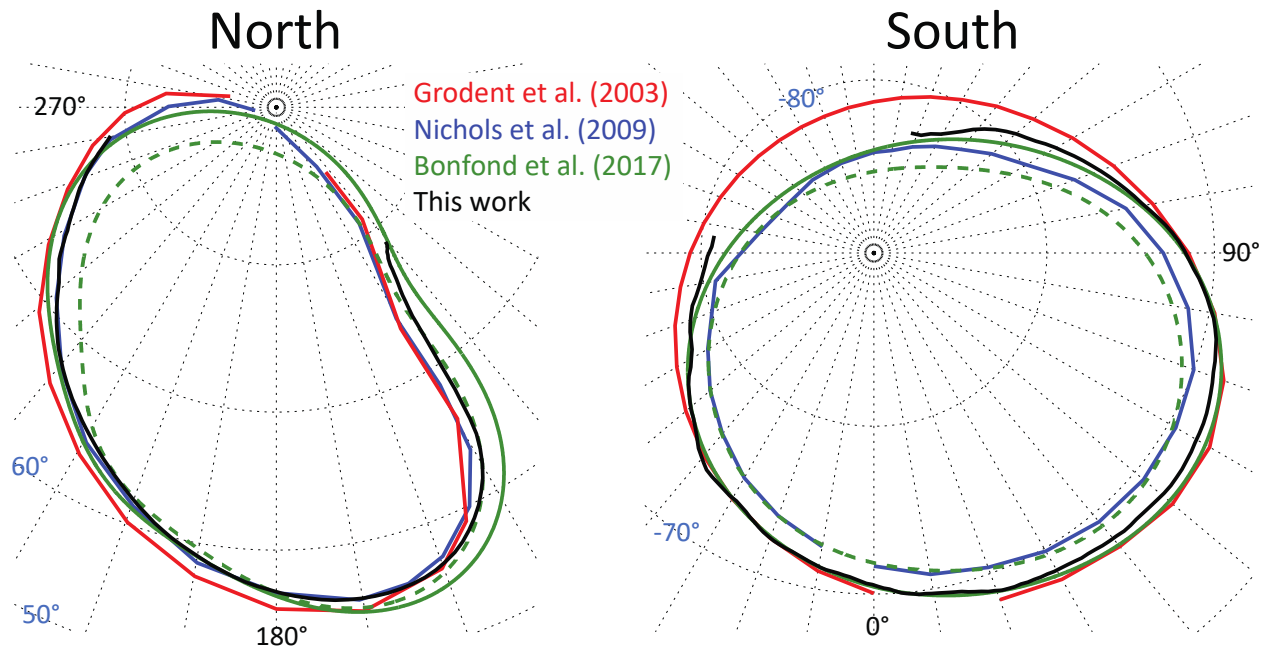
862

863

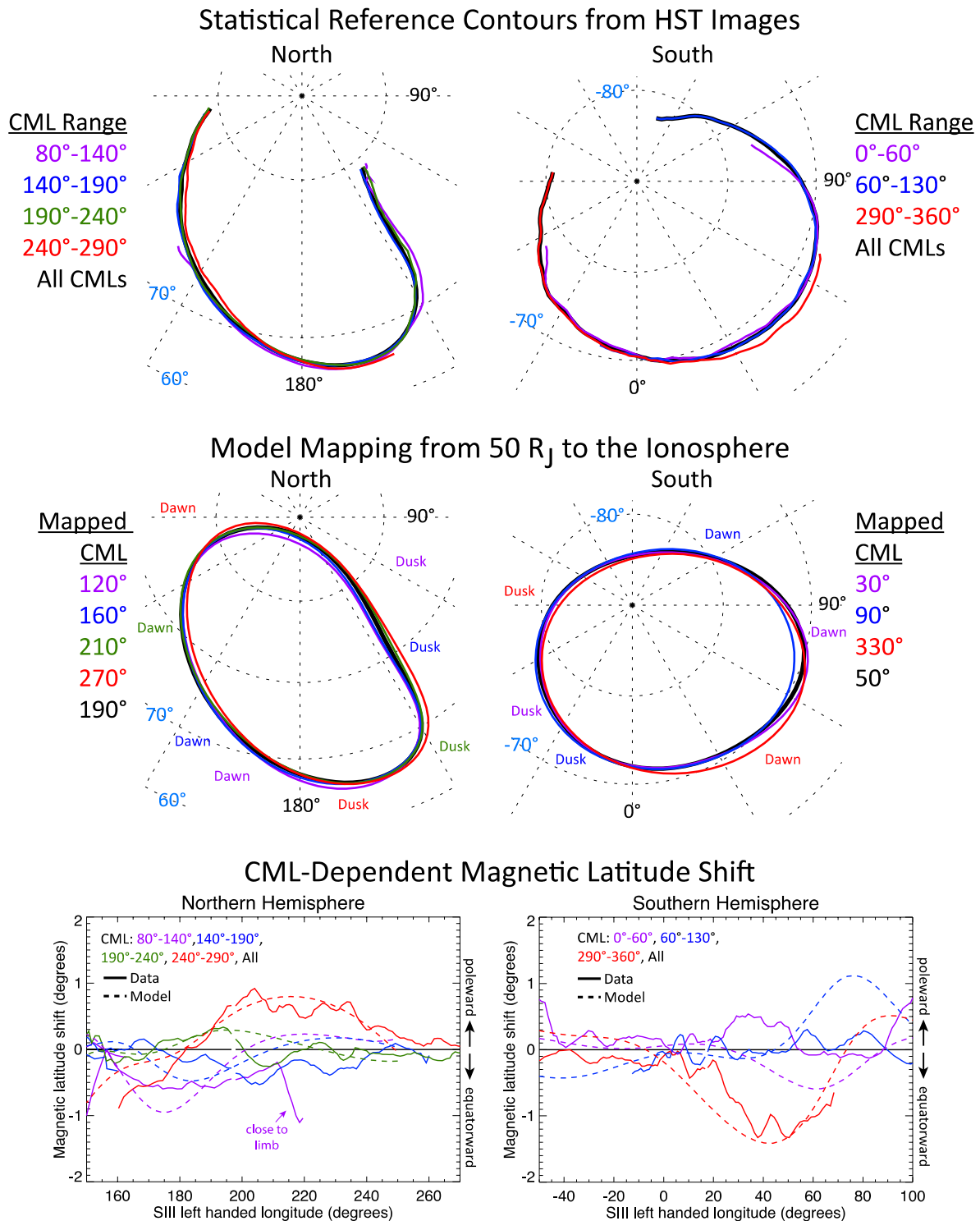
864

**Figure 5.** Distribution of the main emission locations identified following the approach described in Section 3, shown here in a polar view looking down on the planet in the northern hemisphere and looking up at the planet in the southern hemisphere. Colors represent the number of images for which the main emission is located in each  $2^\circ$  magnetic longitude by  $0.1^\circ$  magnetic longitude box. Data are plotted separately for all images (left column) and for images from the

865 specified CML ranges. Thick gray contours in all panels show the reference contours of Nichols  
866 et al. (2009) in the northern hemisphere and Grodent et al. (2003) in the southern hemisphere.  
867 Thick black lines show the statistical main emission reference contour defined in this study using  
868 images from all CMLs.  
869



870  
871 **Figure 6.** Polar plots comparing the location of our statistical reference main emission contour  
872 (black) to the locations of the previous reference contours identified by Grodent et al. (2003)  
873 (red), Nichols et al. (2009) (blue), and Bonfond et al. (2017) (green dashed and solid lines for the  
874 contracted and expanded reference contours, respectively). The left panel shows the reference  
875 contours for the northern hemisphere and the right panel shows the reference contours for the  
876 southern hemisphere.  
877



878

879 **Figure 7.** (top) Polar projections of the statistical reference contours derived for various CML

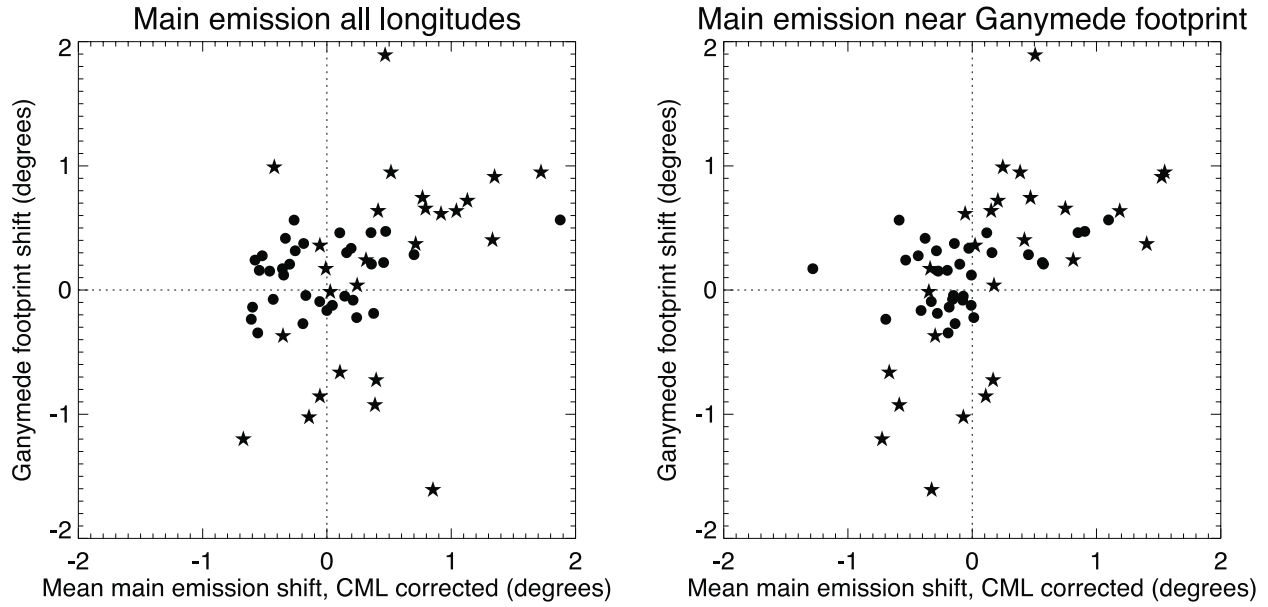
880 bins. In the northern hemisphere the CML bins are 80°-140° (purple), 140°-190° (blue), 190°-

881 240° (green), and 240°-290° (red), and in the southern hemisphere the CML ranges are 0°-60°  
882 (purple), 60°-130° (blue), and 290°-360° (red). Our statistical reference emissions for all images  
883 (from all CMLs) are plotted in black. (middle) Ionospheric contours mapping to 50 R<sub>J</sub> in the  
884 magnetosphere using the Vogt et al. (2011) flux mapping model with JRM09 as the internal field  
885 model, calculated for CML 120° (purple), 160° (blue), 210° (green), and 270° (red) in the  
886 northern hemisphere, and 30° (purple), 90° (blue), and 330° (red) in the southern hemisphere.  
887 Black contours show the ionospheric mapping for CML 190° in the northern and 50° in the  
888 southern hemisphere. (bottom) Magnetic latitudinal shift between the CML-specific reference  
889 contour and the average statistical main emission contour plotted as a function of SIII left handed  
890 longitude. Solid lines show the observed latitudinal shift and dashed lines show the latitudinal  
891 shift predicted from the mapping model.

892

893

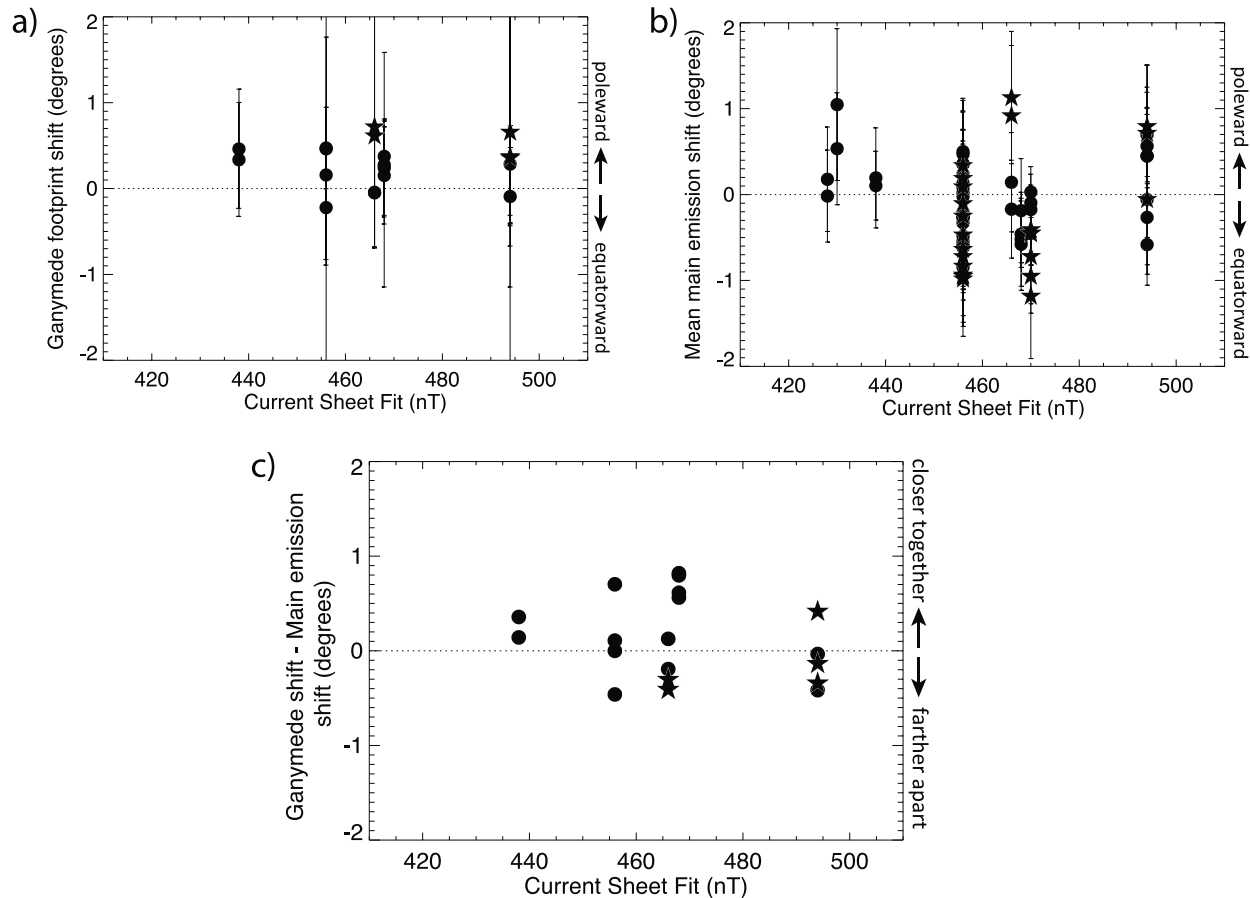
894



895

896 **Figure 8.** Plots of the Ganymede footprint shift and main auroral emission shift. The auroral  
897 shifts are calculated as the mean spherical distance between the respective auroral feature  
898 (footprint or main emission) and a specific reference contour (see text) and are defined as  
899 positive for a poleward shift. In the left panel the main auroral emission shift is calculated using  
900 the main emission position at all longitudes and in the right panel the main auroral emission shift  
901 is calculated using only longitudes near the Ganymede footprint (see text). Circles and stars  
902 indicate northern and southern hemisphere images respectively.

903



904

905 **Figure 9.** Dependence of the observed auroral shifts on the best fit current sheet current density

906 term  $\mu_0 I_0$ , obtained from Galileo data, for the date of each HST image. In all panels circles and

907 stars indicate northern and southern hemisphere images respectively. a) The Ganymede footprint

908 shift as a function of the best fit  $\mu_0 I_0$  for each HST image. Error bars indicate the uncertainty in

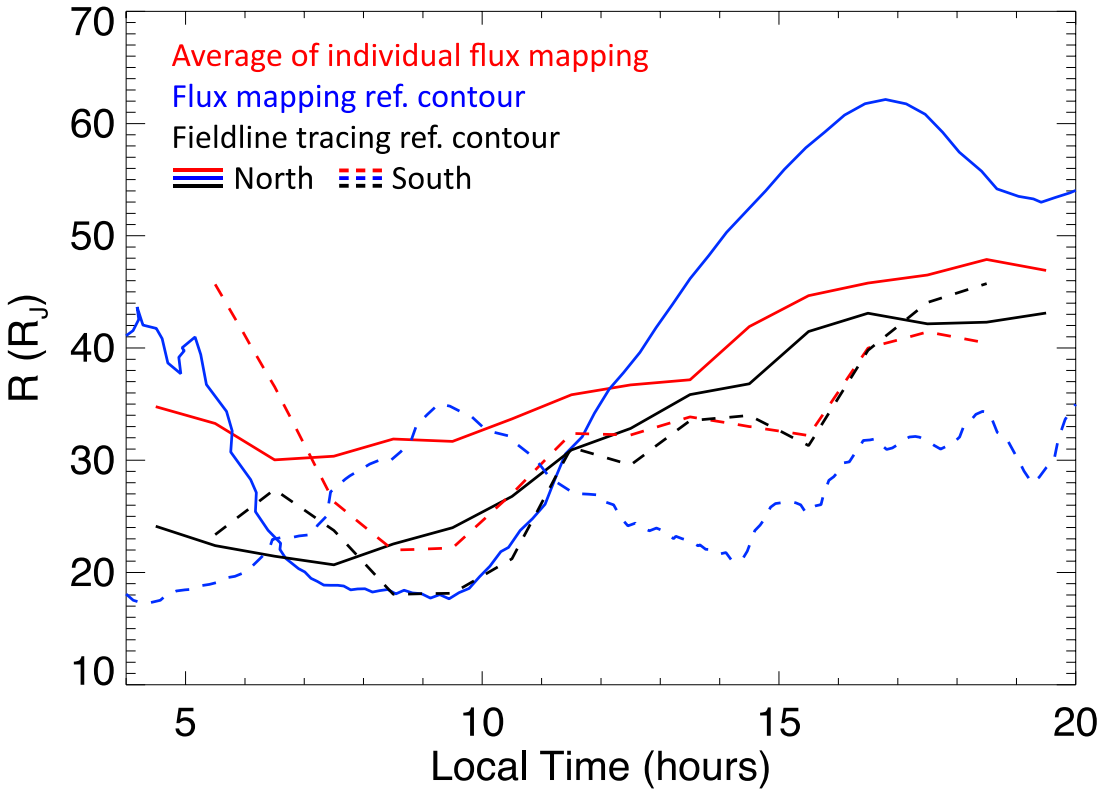
909 the Ganymede footprint position reported by Bonfond et al. (2017) (see text). b) As in Figure 9a

910 but for the CML-corrected main auroral emission shift. Error bars indicate the standard deviation

911 of the main emission shift. c) The difference between the Ganymede footprint shift and the main

912 emission shift as a function of the best fit  $\mu_0 I_0$  for each image.

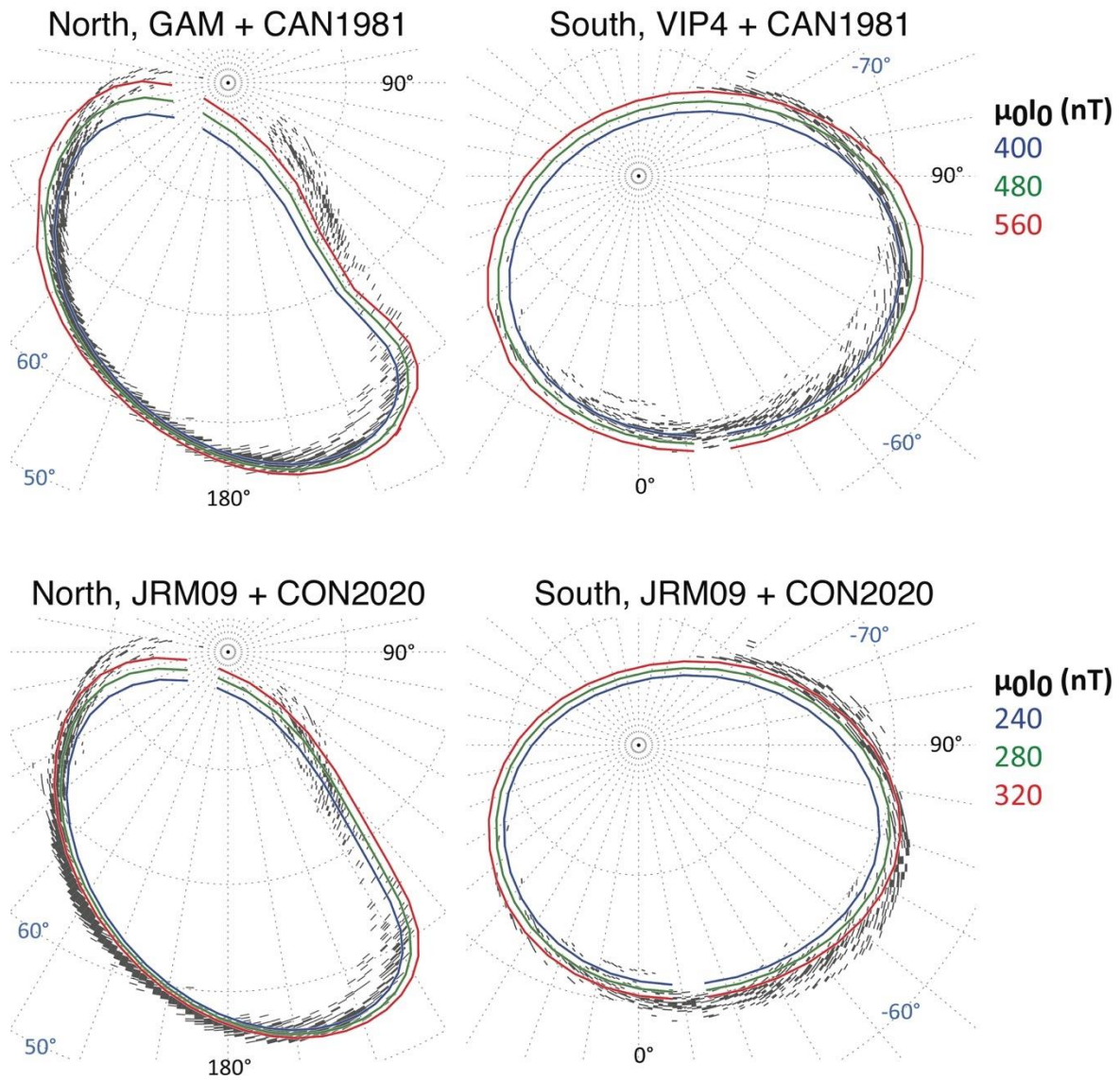
913



914

915 **Figure 10.** The equatorial mapping of Jupiter’s main auroral emission, shown here by the  
 916 mapped radial distance plotted as a function of the mapped local time. Red lines show the result  
 917 of averaging the flux mapping of each individual main emission contour from all images in this  
 918 study, plotted separately for the north (solid) and south (dashed). Blue lines show the flux  
 919 mapping results for the north (solid) and south (dashed) statistical reference contours, calculated  
 920 using the average CML value of the images from each respective hemisphere ( $190^\circ$  for the north  
 921 and  $50^\circ$  for the south). Black lines show the average of the individual mappings for each image  
 922 obtained by tracing field lines using the JRM09 + CAN2020 model (Connerney et al., 2018,  
 923 2020) for the north (solid) and south (dashed).

924



925

926

927

928

929

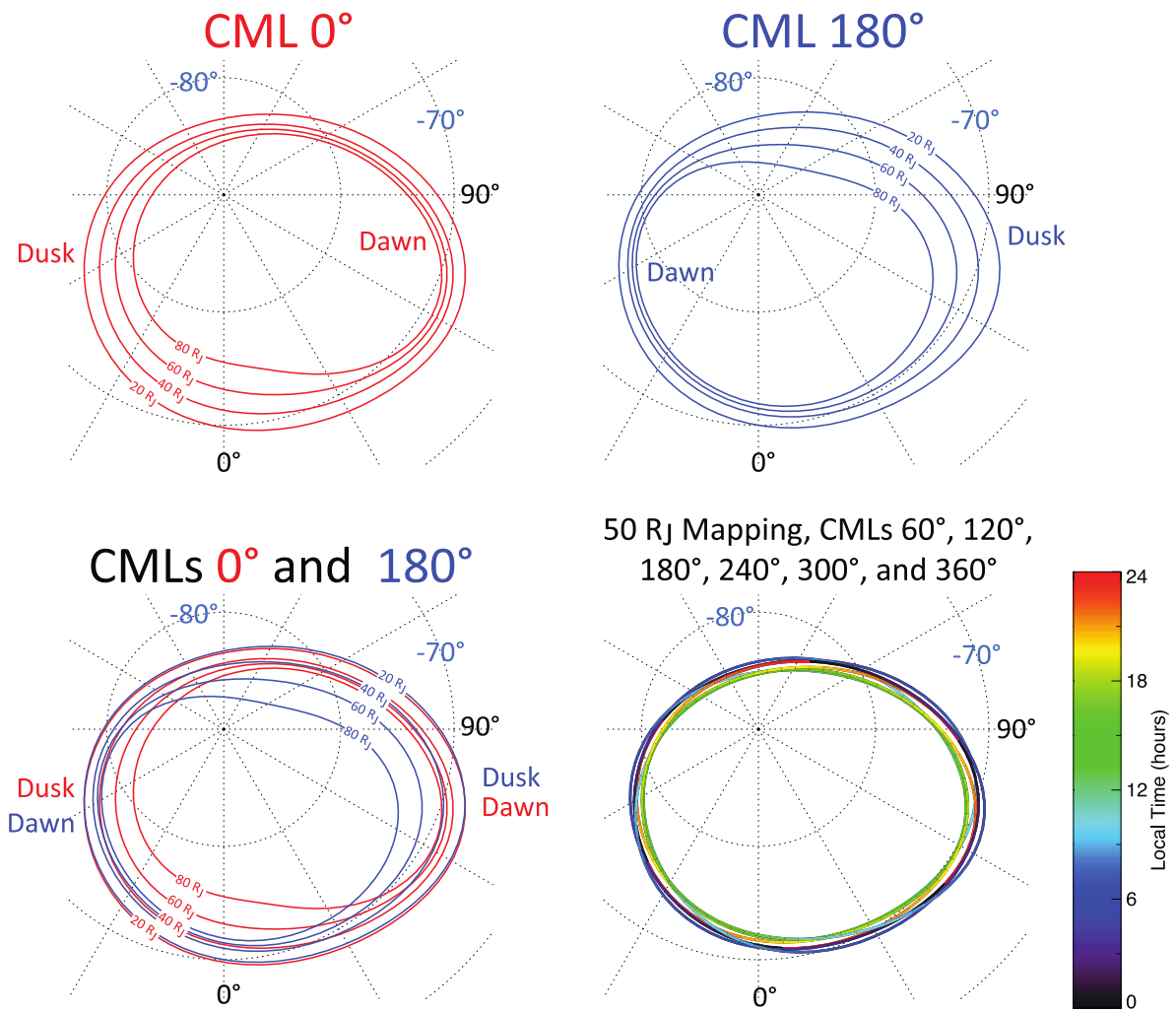
930

931

932

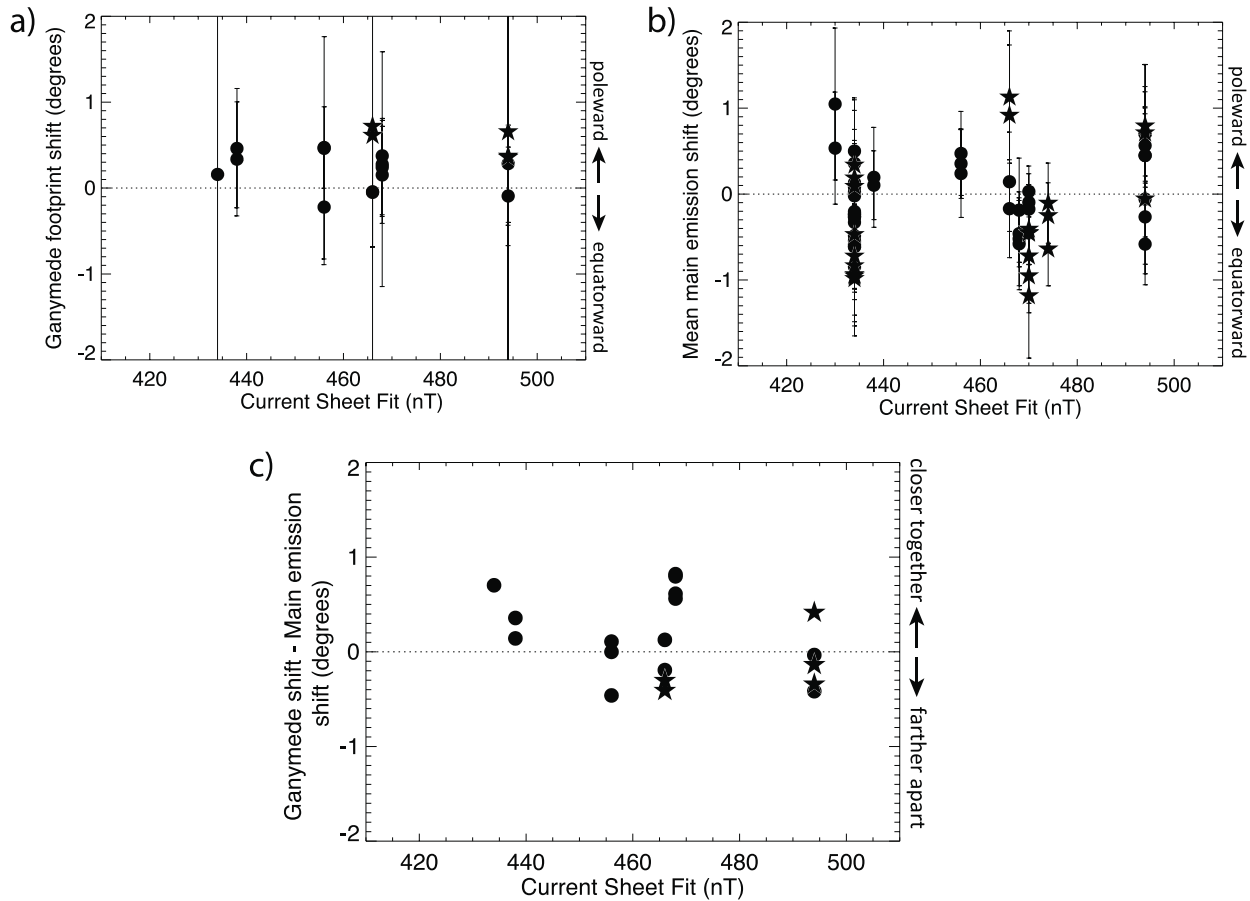
**Figure 11.** Expected variability in the ionospheric mapping of 30 R<sub>J</sub> radial distance in the jovigraphic equator, calculated by tracing model field lines for different internal field models (GAM, Grodent et al., 2008b; VIP4, Connerney et al., 1998; JRM09, Connerney et al. 2018) as noted. In the top row field lines were traced assuming the current sheet model of Connerney, Acuña, and Ness (1981), while in the bottom row field lines were traced using the current sheet model of Connerney et al. (2020). Blue, green, and red contours show the traced 30 R<sub>J</sub> mapping calculated using low, average, and high values, respectively, for the  $\mu_0 I_0$  parameter in the

933 CAN1981 (top) and CON2020 (bottom) current sheet models (see text). Bins of  $2^\circ$  magnetic  
 934 longitude by  $0.1^\circ$  magnetic latitude are shaded in gray if the main emission was located in that  
 935 area in at least two of the images used in this study.  
 936



937  
 938 **Figure S1.** Ionospheric mapping contours from the Vogt et al. (2011) flux mapping model with  
 939 JRM09 as the internal field model. (top left) Contours mapping to equatorial radial distances 20-,  
 940 40, 60, and 80 R<sub>J</sub> at CML 0°. (top right) Contours mapping to equatorial radial distances 20, 40,  
 941 60, and 80 R<sub>J</sub> at CML 180°. (bottom left) Overlap of the CML 0° (red) and CML 180° (blue)

942 mapping contours from the top row. (bottom right) Contours mapping to 50 R<sub>J</sub> in the equator  
 943 using the mapping model every 60° CML from 60° to 360°, colored by the mapped local time.  
 944



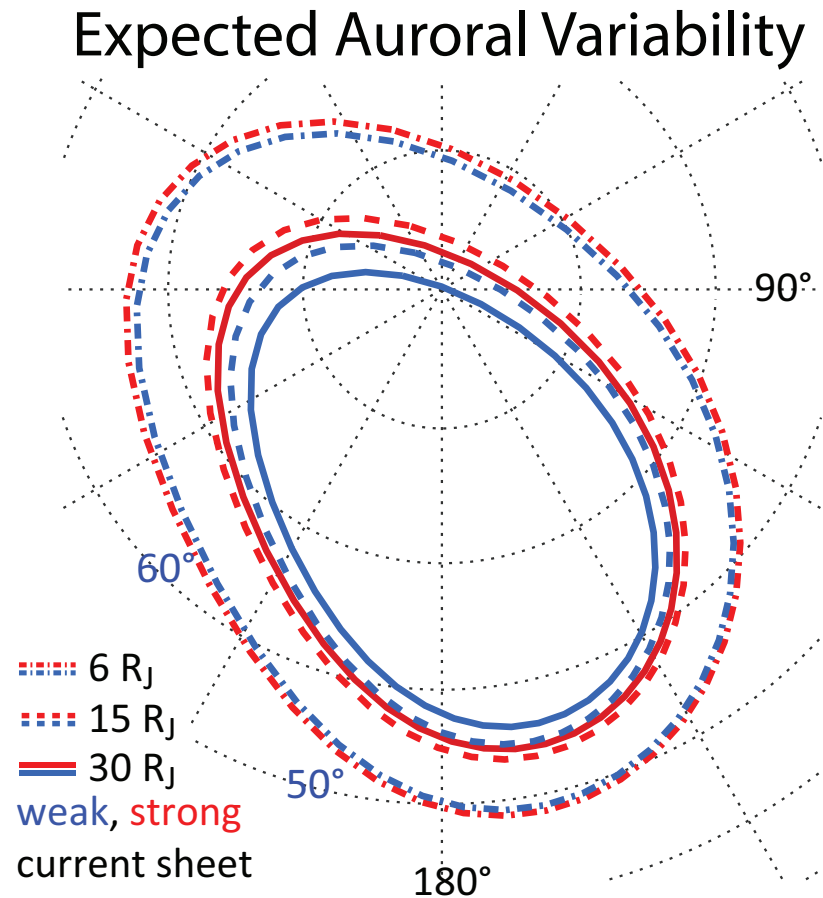
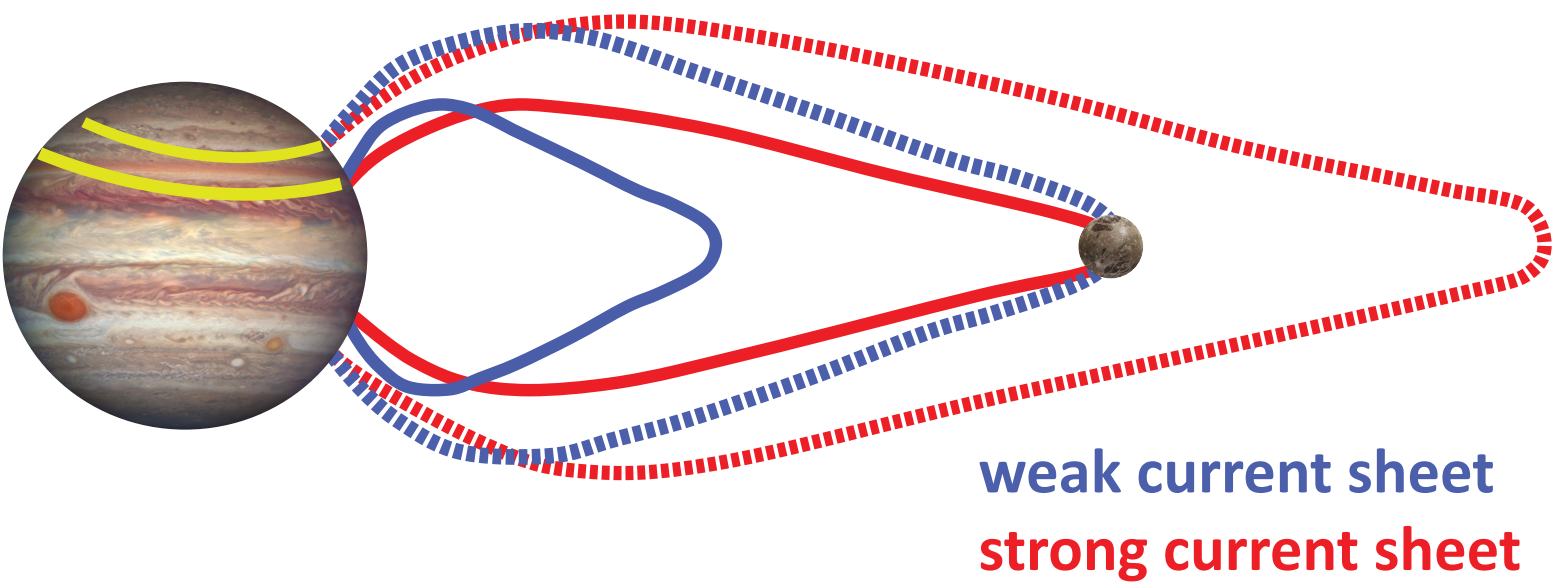
945  
 946 **Figure S2.** Dependence of the observed auroral shifts on the best fit current sheet current density  
 947 term  $\mu_0 I_0$ , obtained from Galileo data, for the date of each HST image. This figure follows the  
 948 format of Figure 9 except that here we plot the best fit  $\mu_0 I_0$  values from the inbound or outbound  
 949 orbit segments corresponding to each HST image date where applicable rather than the orbit-  
 950 averaged  $\mu_0 I_0$  fit. In all panels circles and stars indicate northern and southern hemisphere  
 951 images respectively. a) The Ganymede footprint shift as a function of the best fit  $\mu_0 I_0$  for each  
 952 HST image. Error bars indicate the uncertainty in the Ganymede footprint position reported by  
 953 Bonfond et al. (2017). b) As in Figure S2a but for the CML-corrected main auroral emission

954 shift. Error bars indicate the standard deviation of the main emission shift. c) The difference  
955 between the Ganymede footprint shift and the main emission shift as a function of the best fit  
956  $\mu_0 I_0$  for each image.

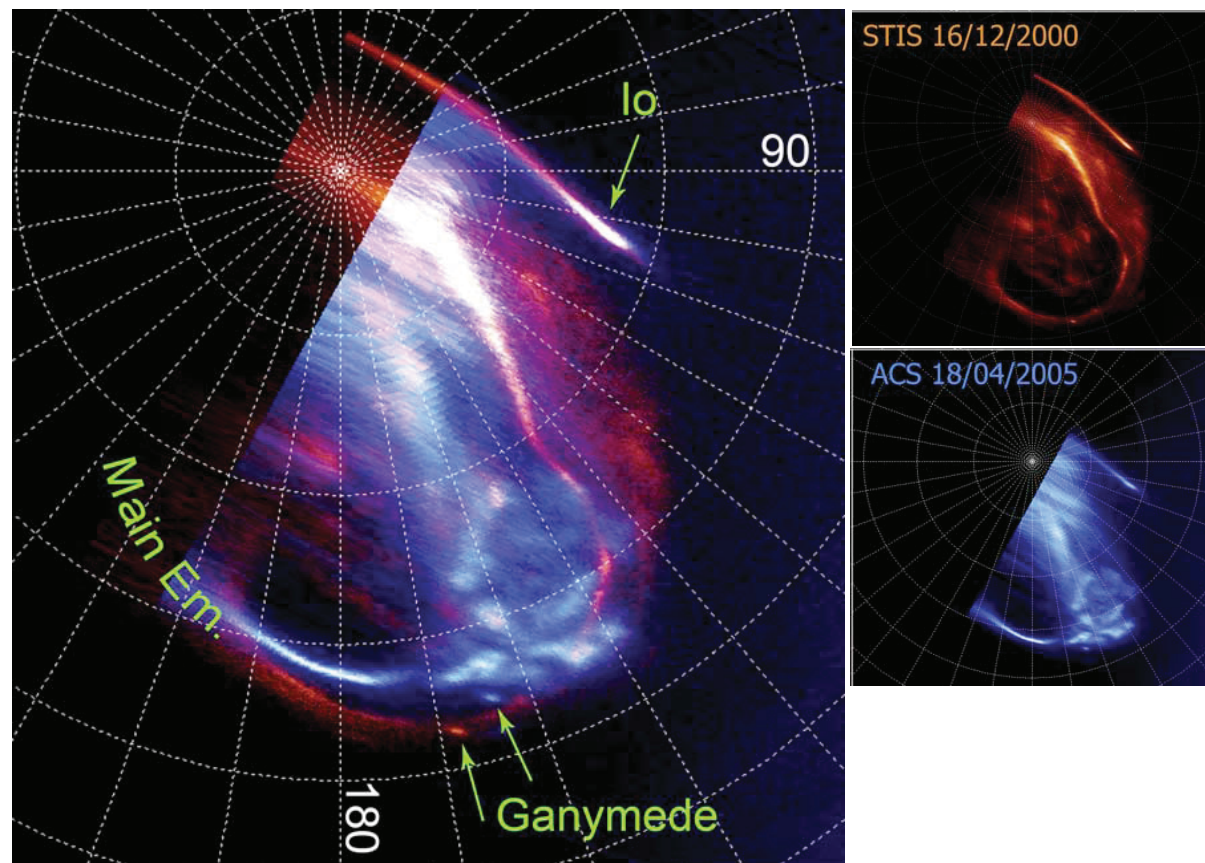
957

958 **Table S1.** (see separate file) Date, time, CML, and other relevant details for the 143 images used  
959 in this study.

Figure 1.



Main Emission and Ganymede footprint  
both move in latitude



Main Emission moves;  
Ganymede footprint does not

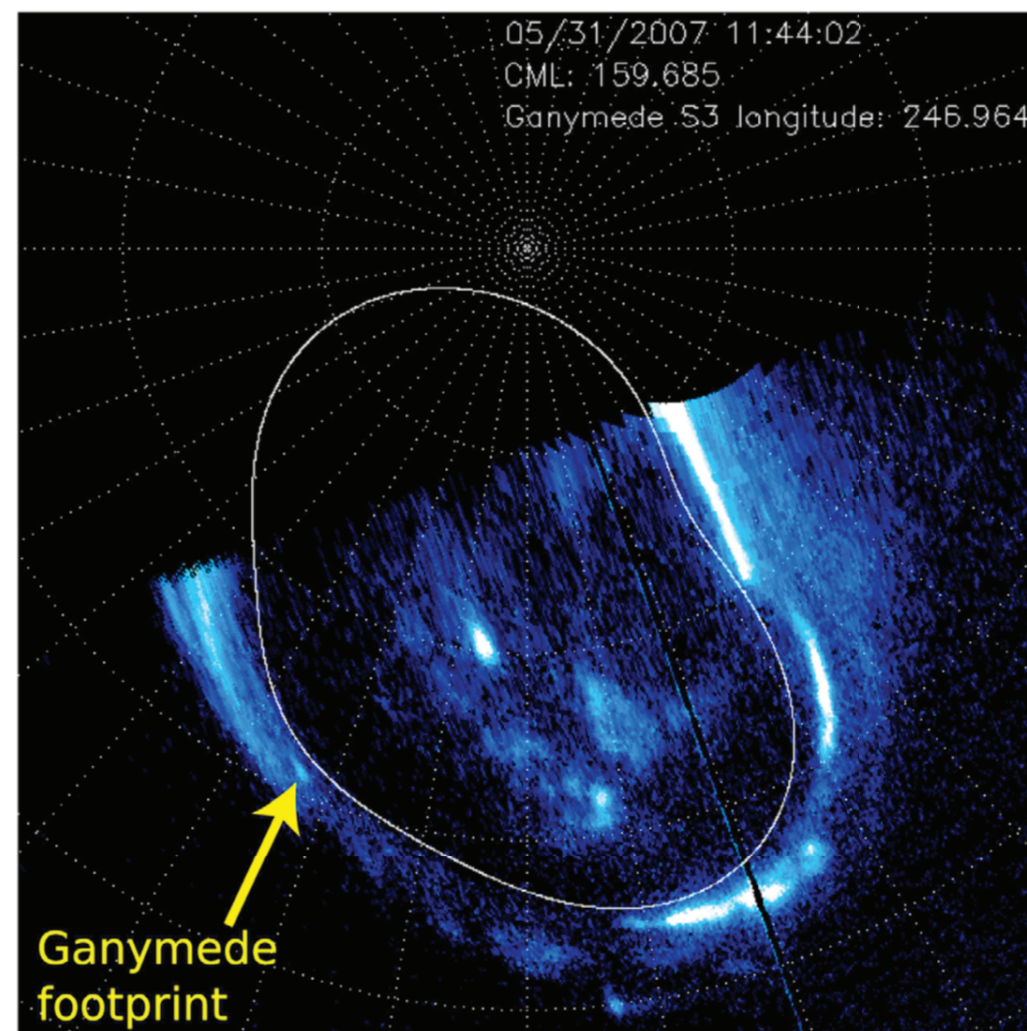


Figure 2.

# Galileo's position during HST images

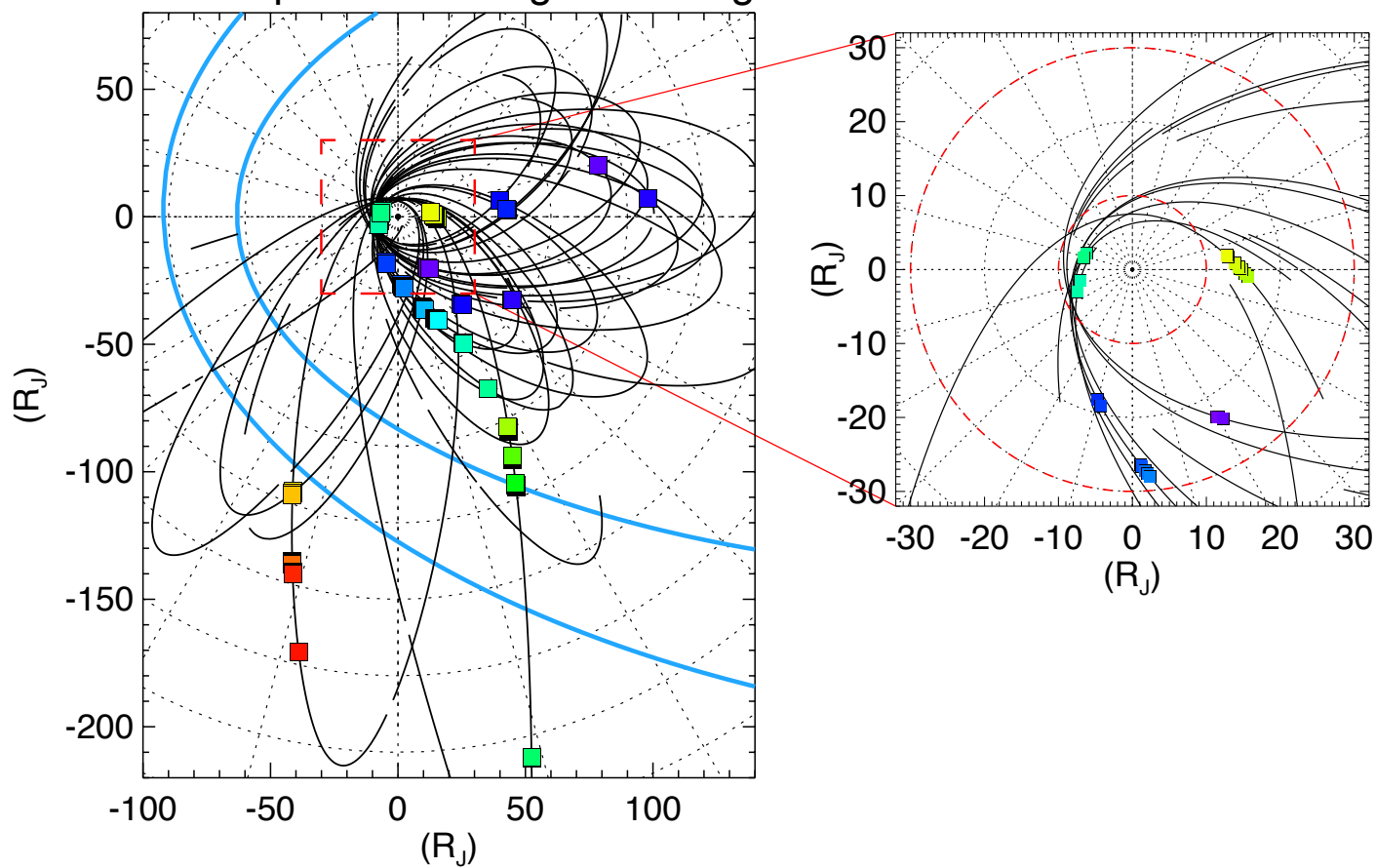
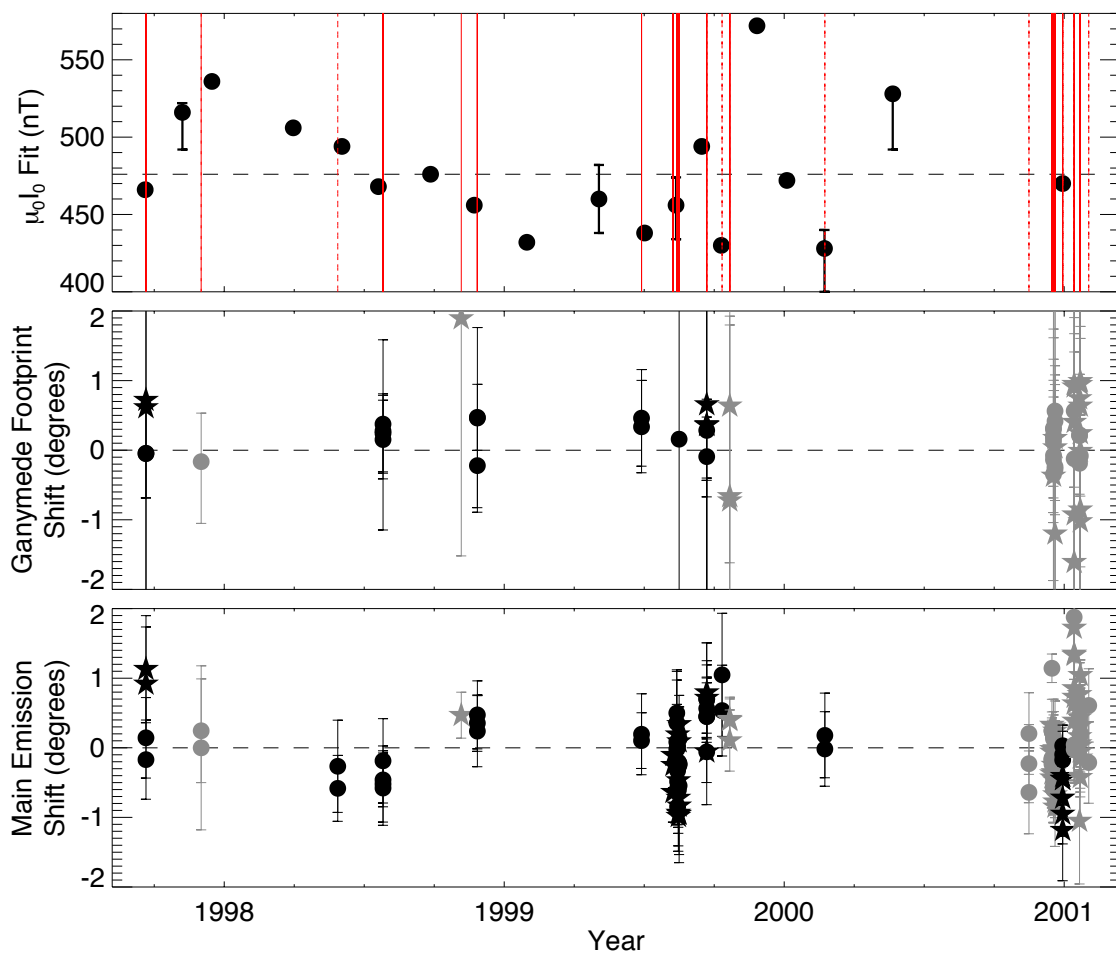


Figure 3.



**Figure 4.**

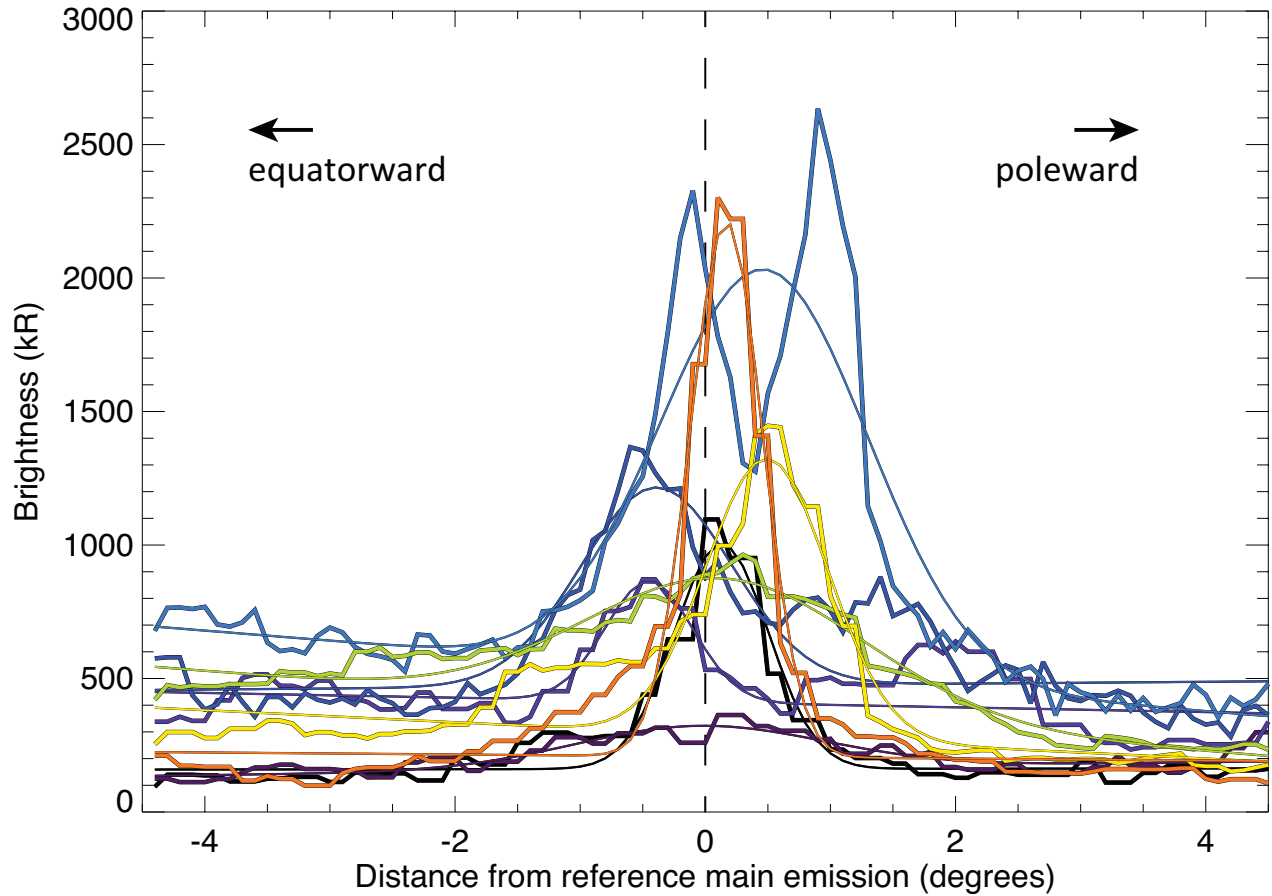
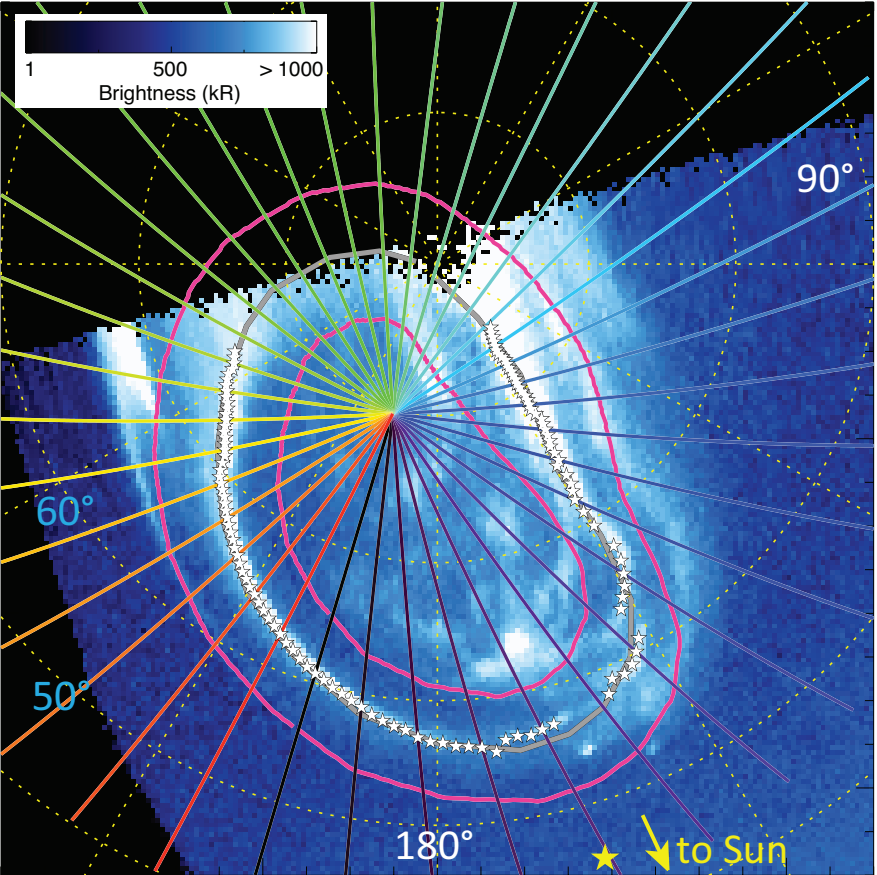
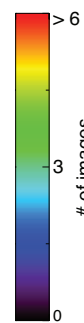
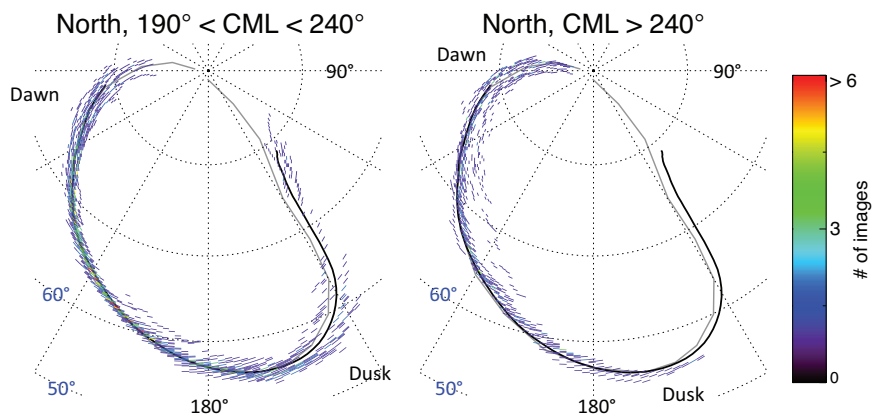
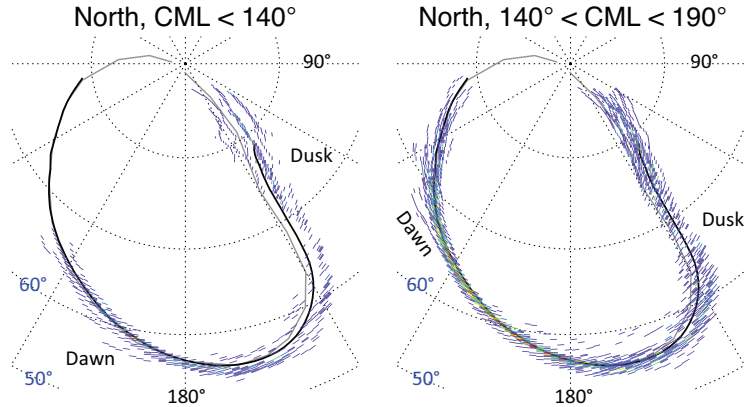
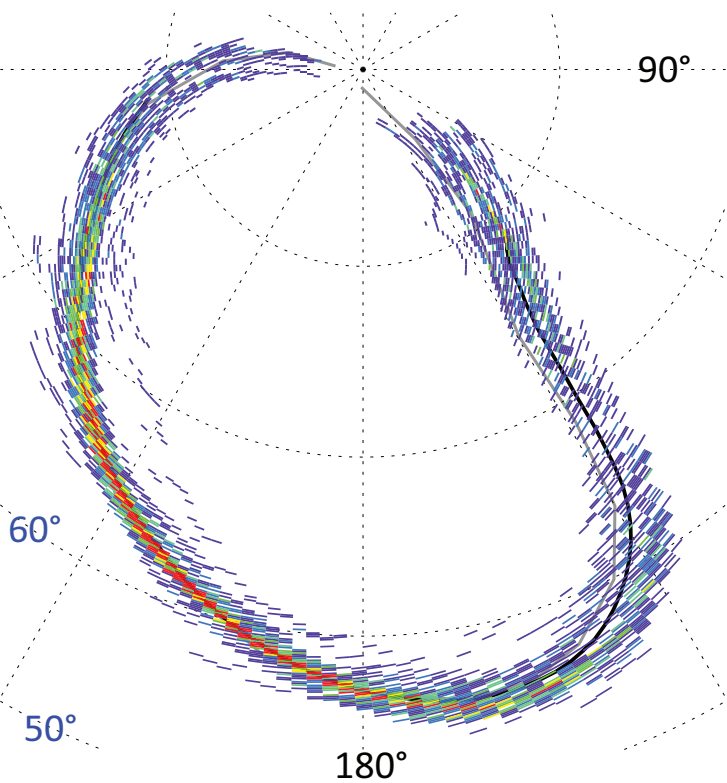


Figure 5.

# North, All CMLs



# South, All CMLs

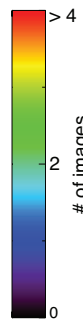
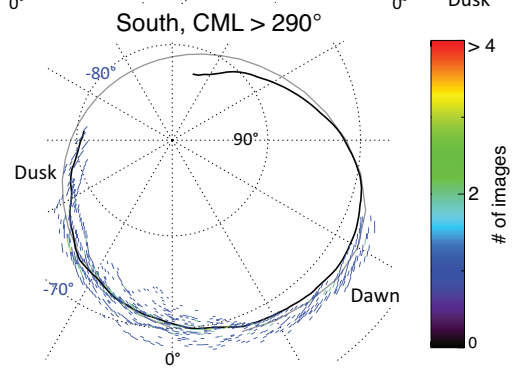
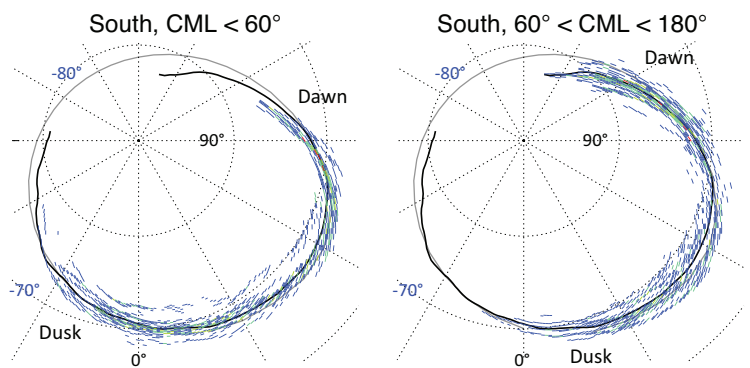
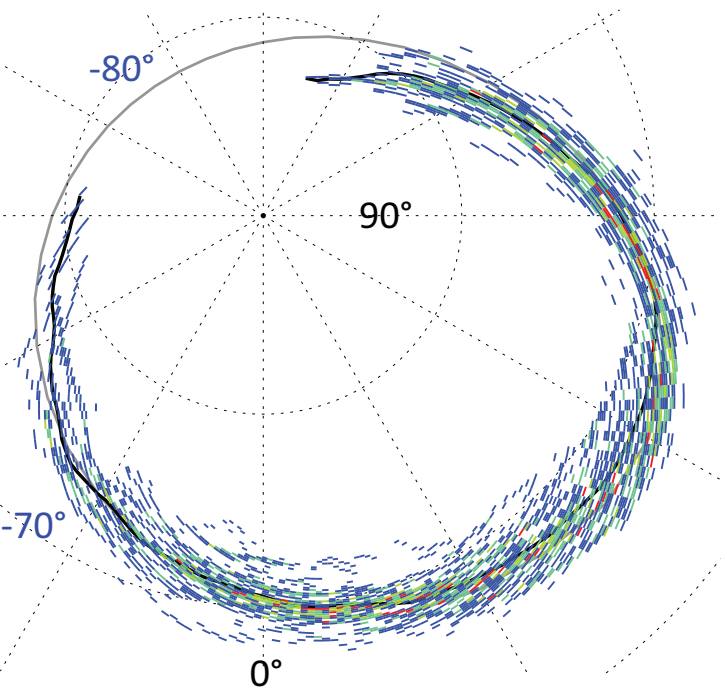
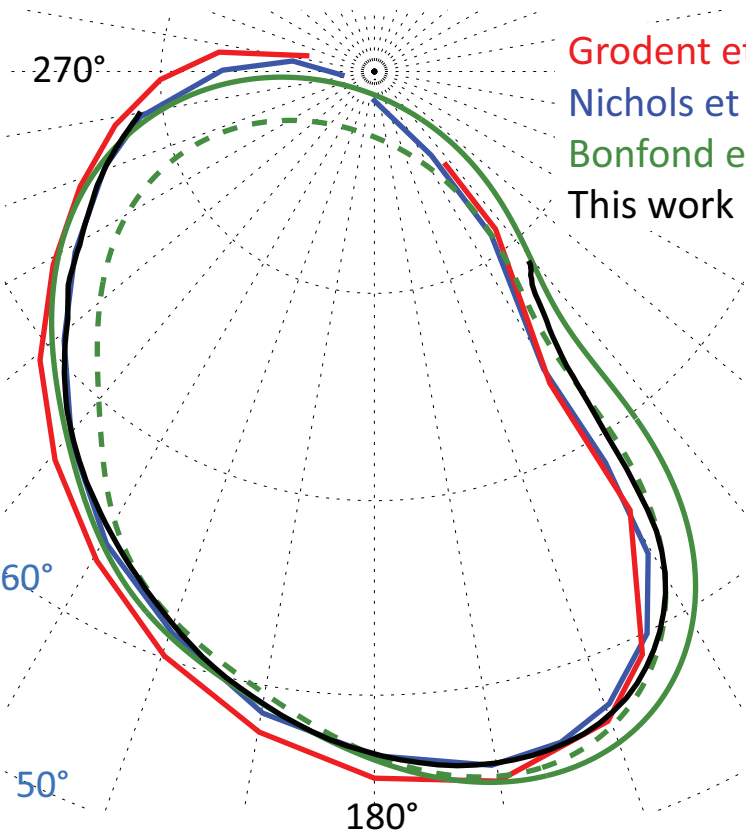


Figure 6.

# North



Grodent et al. (2003)

Nichols et al. (2009)

Bonfond et al. (2017)

This work

# South

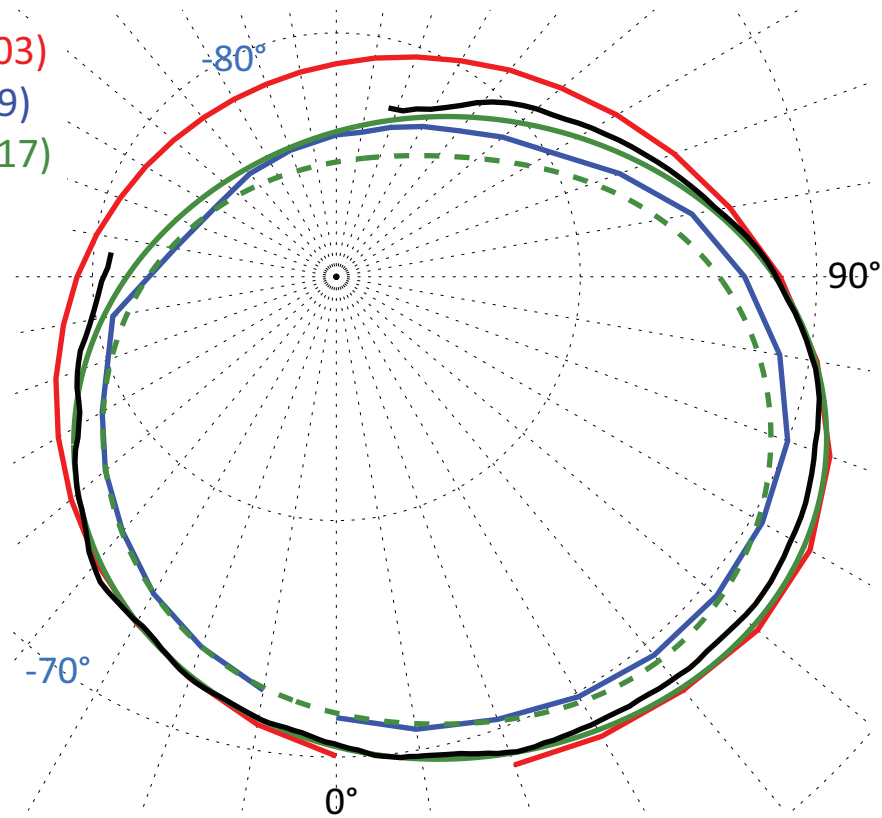
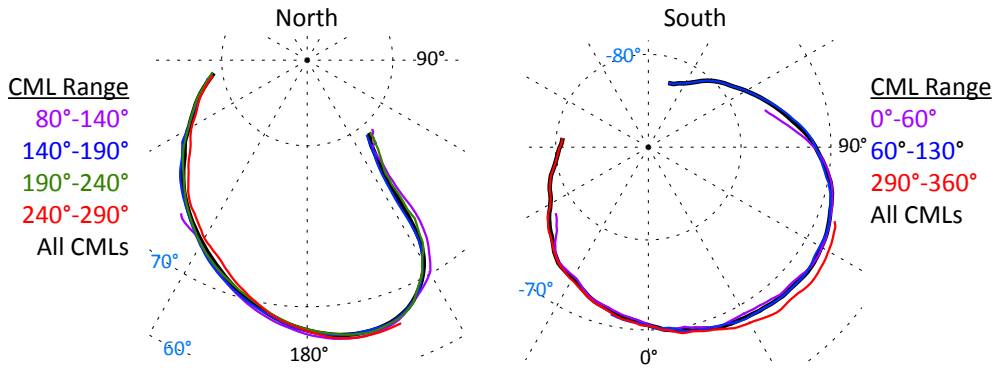
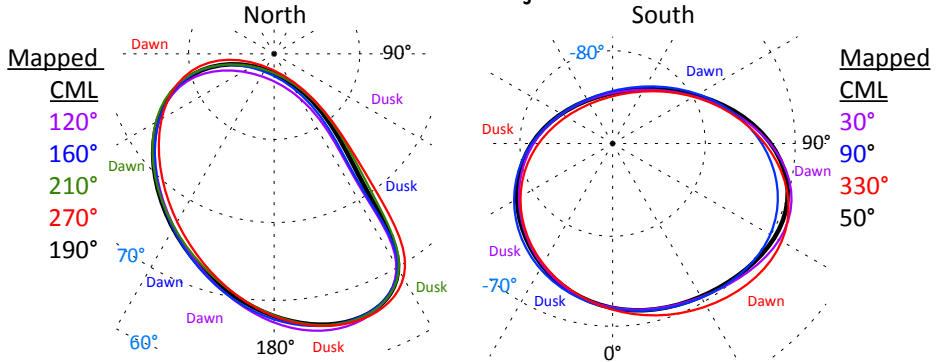


Figure 7.

# Statistical Reference Contours from HST Images



# Model Mapping from 50 R<sub>J</sub> to the Ionosphere



# CML-Dependent Magnetic Latitude Shift

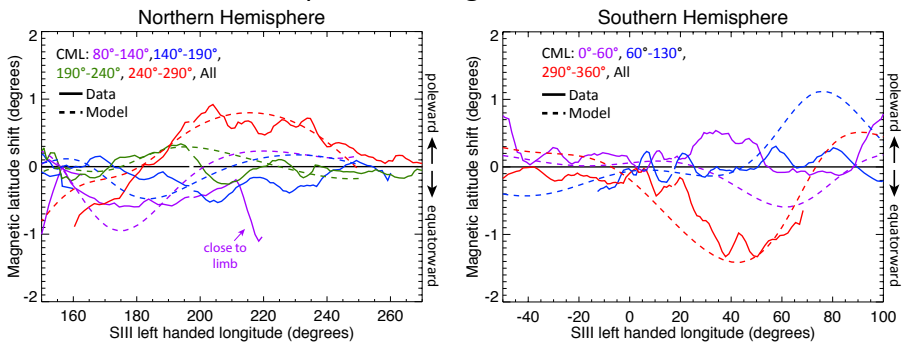
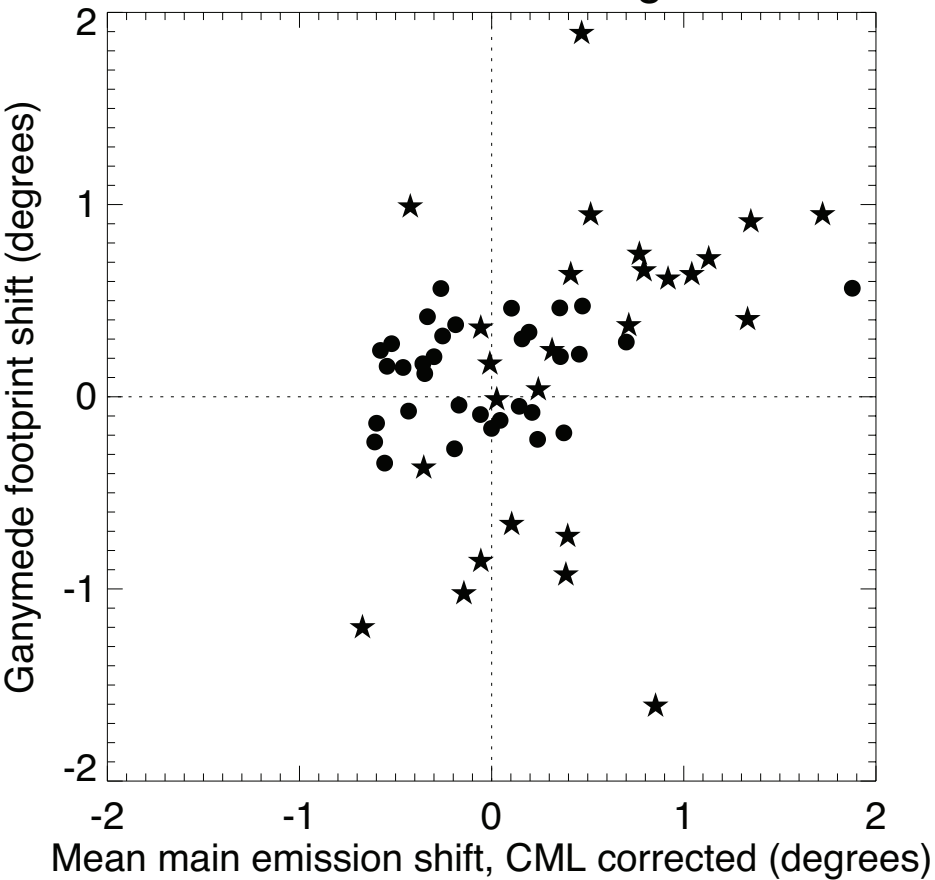


Figure 8.

Main emission all longitudes



Main emission near Ganymede footprint

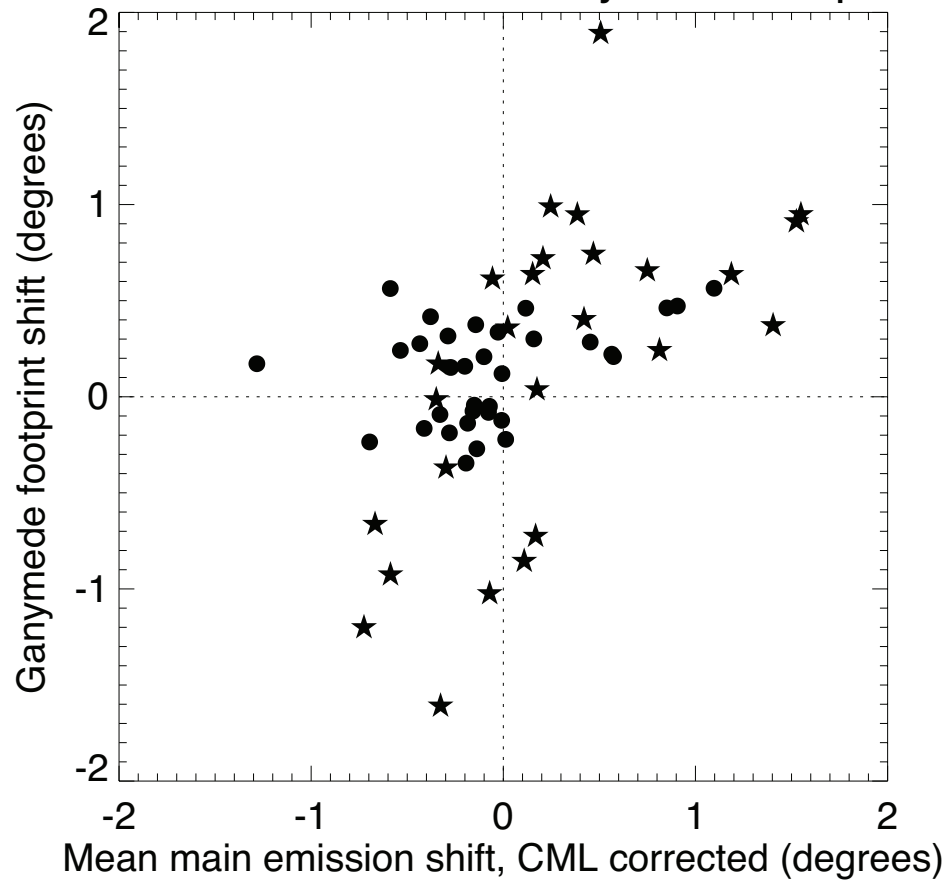


Figure 9.

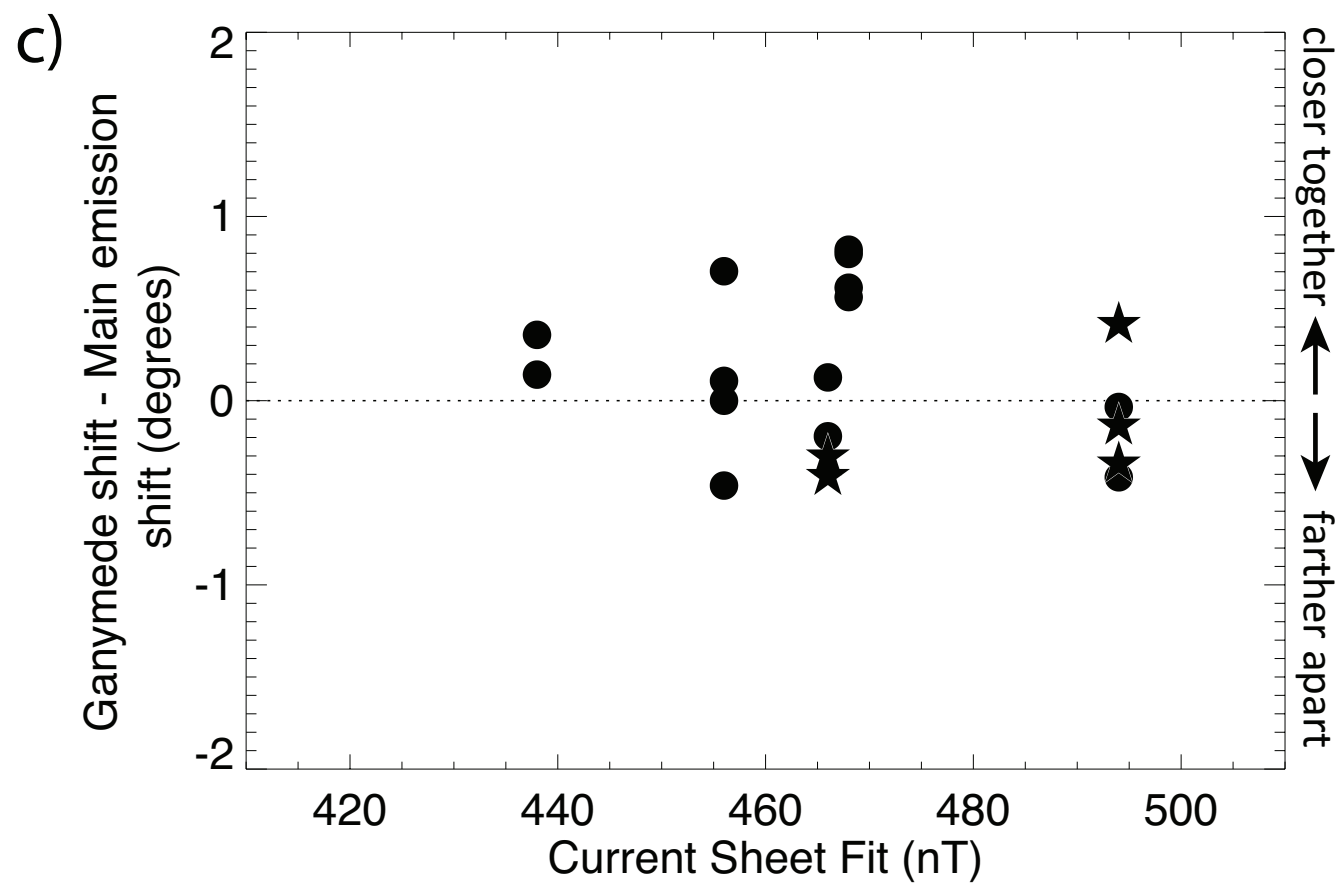
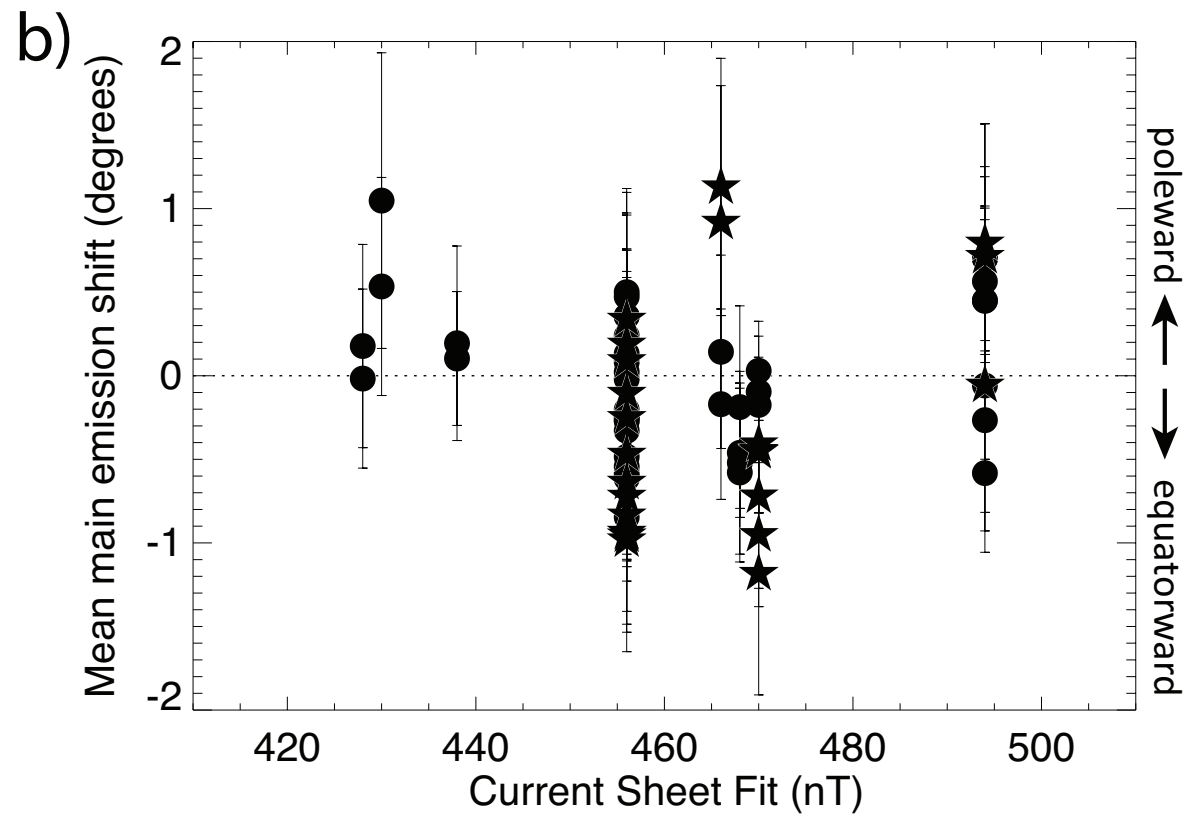
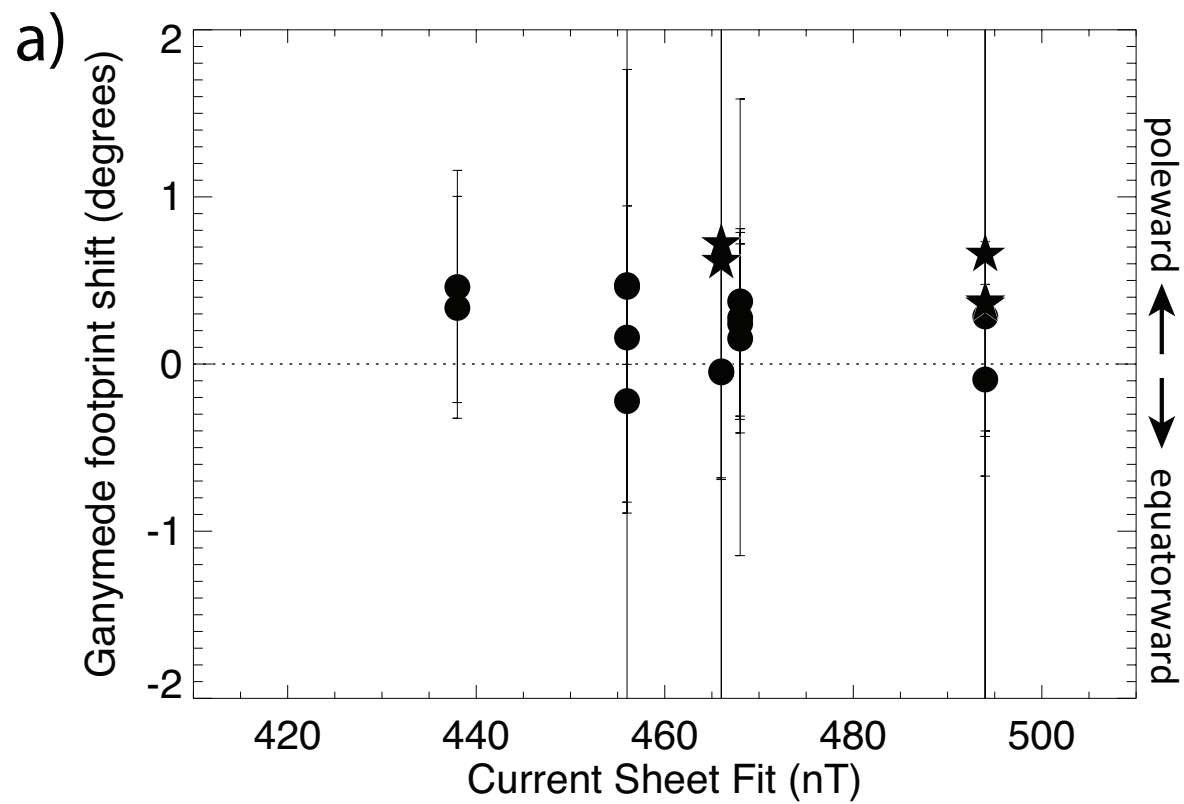


Figure 10.

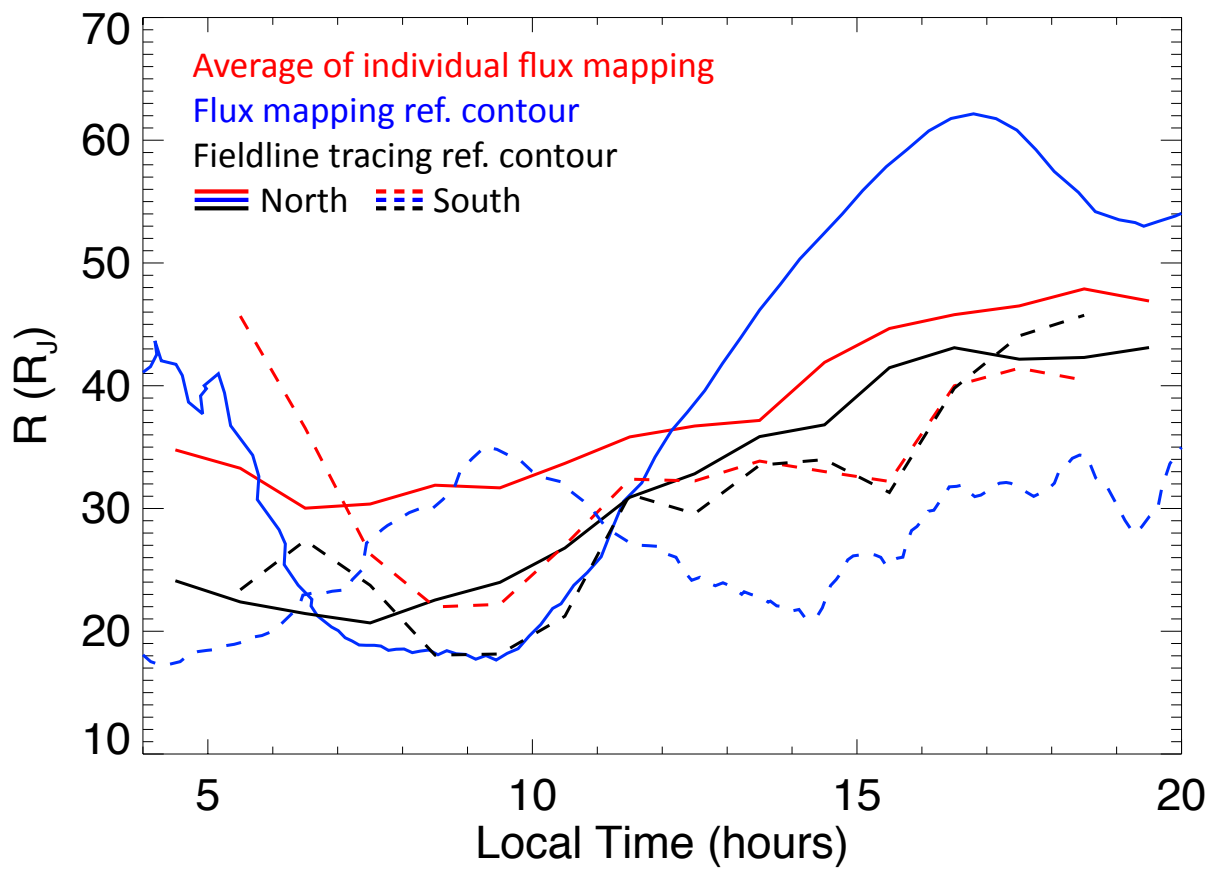
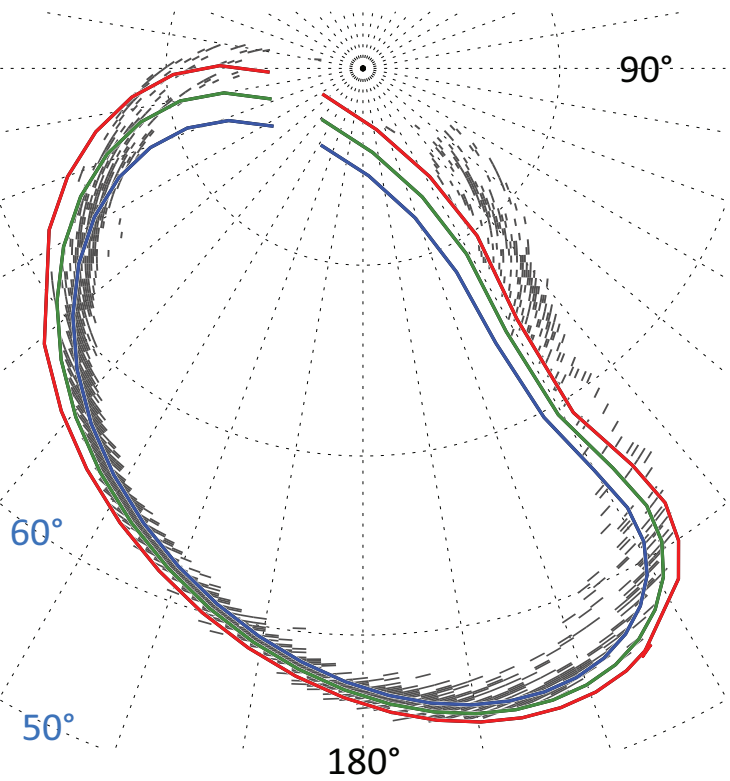
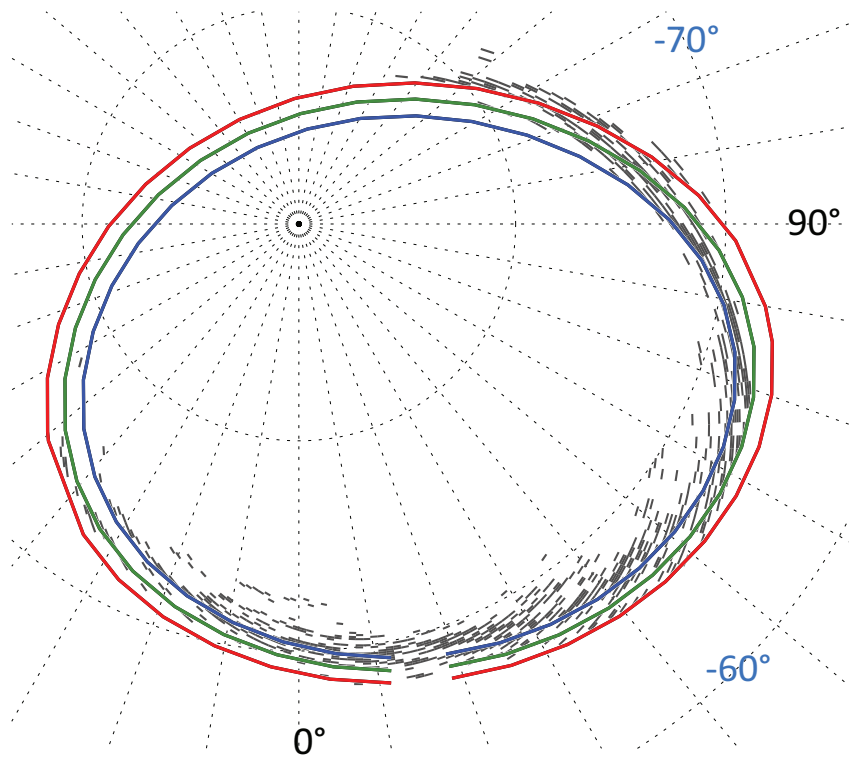


Figure 11.

North, GAM + CAN1981

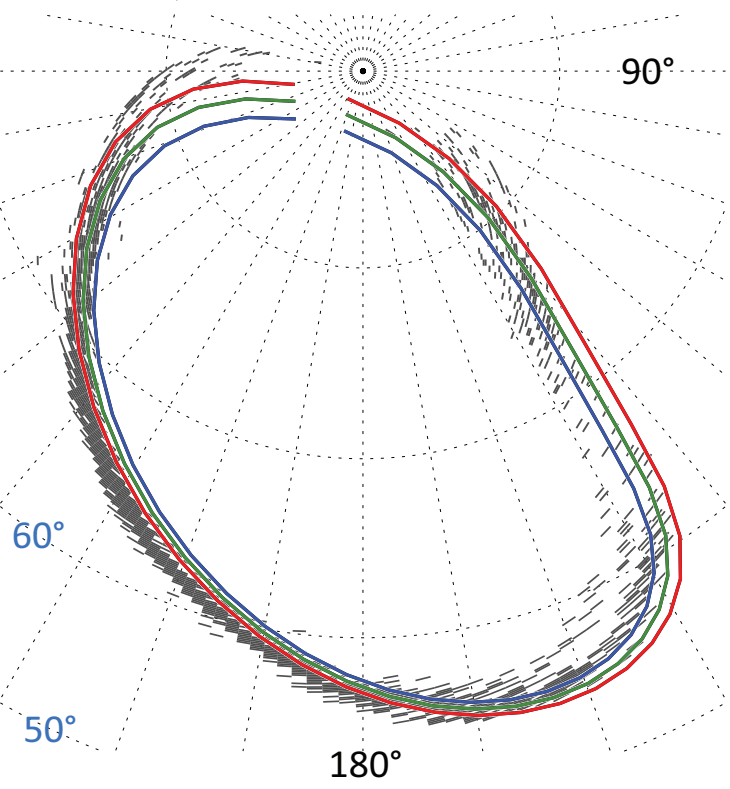


South, VIP4 + CAN1981

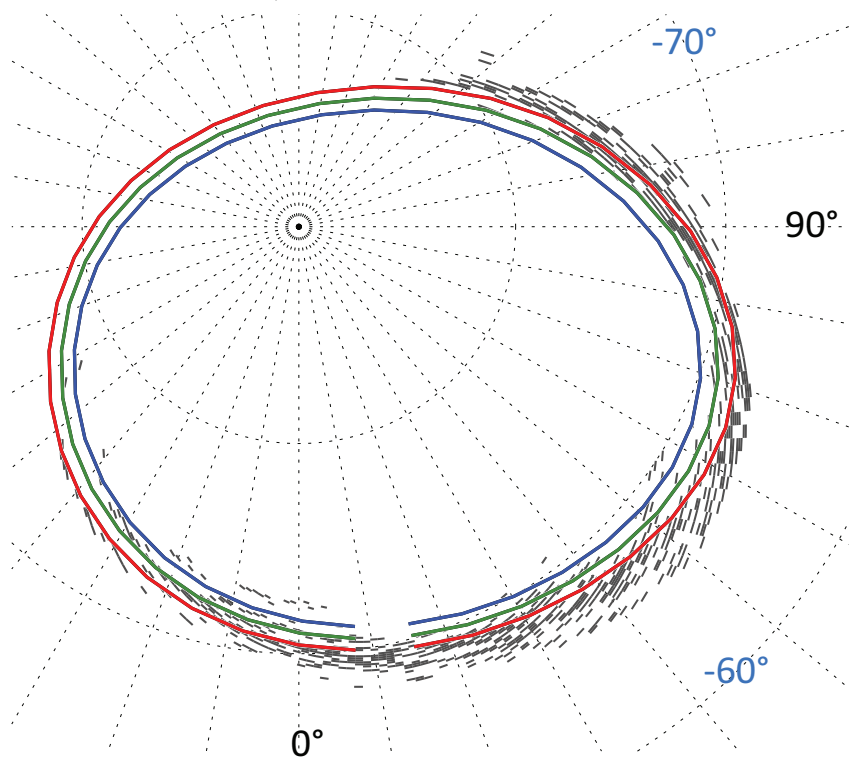


$\mu_0 I_0$  (nT)  
400  
480  
560

North, JRM09 + CON2020



South, JRM09 + CON2020



$\mu_0 I_0$  (nT)  
240  
280  
320

Year	Day of Year	Time (hh:mm:ss)	Rootname	Hemisphere	CML (degrees)	Ganymede fo
1997	263	13:58:28	o43b06btq	South	85.27	Yes
1997	263	14:05:08	o43b06bvq	South	89.3002	Yes
1997	263	15:35:15	o43b05c1q	North	143.7794	Yes
1997	263	15:41:55	o43b05c3q	North	147.8096	Yes
1997	335	4:06:06	o43b09b3q	North	117.5941	Yes
1997	335	4:17:06	o43b09b5q	North	123.3356	No
1998	148	11:58:04	o43b20010	North	162.9034	No
1998	148	12:21:59	o43b20x9q	North	180.2019	No
1998	207	13:49:01	o43b12xaq	North	110.2241	Yes
1998	207	14:27:01	o43b2rxeq	North	133.7433	Yes
1998	207	15:23:32	o43b2sxxq	North	166.9409	Yes
1998	207	15:30:14	o43b2sxiiq	North	171.0573	Yes
1998	309	4:26:00	o43b15xeq	South	14.0346	Yes
1998	330	0:51:55	o43b13s8q	North	164.2251	Yes
1998	330	0:58:08	o43b13saq	North	168.1843	Yes
1998	330	2:37:30	o43b4askq	North	227.9448	Yes
1999	179	17:04:22	o43b21010	North	162.6151	Yes
1999	179	17:24:30	o43b21020	North	175.3293	Yes
1999	220	11:35:22	o5hya3z9q	South	13.2715	No
1999	220	12:56:47	o5hyc3zhq	South	62.7378	No
1999	220	13:39:28	o5hye3zpq	South	88.2966	No
1999	225	13:51:04	o5hy02tsq	North	128.1348	No
1999	225	13:57:39	o5hy02tuq	North	132.8214	No
1999	225	15:26:49	o5hy02u0q	North	186.0218	No
1999	225	15:33:24	o5hy02u2q	North	190.6733	No
1999	226	9:12:43	o5g202x4q	South	110.7551	No
1999	226	9:44:15	o5g2a2010	North	129.5923	No
1999	226	9:52:10	o5g2a2xeq	North	134.6304	No
1999	226	11:01:04	o5g2c2010	North	176.0331	No
1999	226	11:15:16	o5g2c2xprq	North	185.1854	No
1999	226	11:26:16	o5g2c2xrq	North	191.258	No
1999	226	12:37:46	o5g2e2010	North	234.4946	No
1999	226	12:51:58	o5g2e2y2q	North	243.7127	No
1999	226	13:02:58	o5g2e2y4q	North	249.7196	No
1999	227	14:25:12	o5g2a3caq	South	89.921	No
1999	227	14:30:25	o5g2a3cbq	South	93.4729	No
1999	227	14:34:43	o5g2a3cdq	South	96.2413	No
1999	227	14:41:55	o5g2a3cfq	South	100.0274	No
1999	227	14:54:12	o5g2b3chq	North	107.4535	No
1999	227	16:28:02	o5g2d3csq	North	163.9806	No

1999	227	18:04:43	o5g2f3d3q	North	222.4323	No
1999	228	9:45:17	o5g2a1bqq	South	71.2713	No
1999	228	9:50:30	o5g2a1brq	South	74.8232	No
1999	228	9:54:48	o5g2a1btq	South	77.5916	No
1999	228	10:02:00	o5g2a1bvq	South	81.3777	No
1999	228	10:14:17	o5g2b1bxq	North	88.8039	No
1999	228	11:47:35	o5g2d1c3q	North	145.0087	Yes
1999	228	13:24:16	o5g2f1c9q	North	203.4605	No
1999	228	15:02:43	o5g2h1cfq	North	262.9805	No
1999	264	18:56:54	o5hy04hsq	South	68.1017	Yes
1999	264	19:09:34	o5hy04010	South	75.1415	Yes
1999	264	19:30:57	o5hy04i2q	South	88.6356	Yes
1999	264	20:27:30	o5hya4i4q	North	122.7892	Yes
1999	264	20:37:30	o5hya4i6q	North	128.2834	Yes
1999	264	21:04:50	o5hya4iaq	North	145.2913	Yes
1999	264	22:01:54	o5hya4icq	North	179.9357	No
1999	264	22:12:54	o5hya4ieq	North	185.9551	No
1999	264	22:38:52	o5hya4iiq	North	202.6959	No
1999	284	8:07:01	o5hya5bhq	North	168.0855	No
1999	284	9:26:34	o5hya5bpq	North	216.1962	No
1999	294	1:45:14	o5hya1qqq	South	4.0287	Yes
1999	294	3:03:26	o5hya1qqq	South	51.1586	Yes
1999	294	3:41:16	o5hya1qwq	South	74.0202	Yes
2000	53	16:19:51	o5hyb6fzq	North	111.6086	No
2000	53	16:59:32	o5hyb6g7q	North	134.7111	No
2000	319	5:58:28	o5hyb5eiq	North	147.8579	No
2000	319	7:17:59	o5hyb5eqq	North	195.9811	No
2000	319	7:56:31	o5hyb5eyq	North	219.2357	No
2000	349	10:46:42	o6ba02010	North	162.0103	No
2000	349	11:12:02	o6ba02mhq	North	178.1079	No
2000	349	12:05:24	o6ba02020	North	209.5926	No
2000	349	12:13:03	o6ba02mmq	North	214.1675	No
2000	349	13:42:24	o6ba02msq	North	268.2896	No
2000	349	13:46:47	o6ba02030	North	270.7887	No
2000	349	14:13:54	o6ba02n5q	North	288.0991	No
2000	349	15:18:25	o6baa2naq	South	326.3175	No
2000	349	15:58:40	o6baa2ngq	South	350.6528	No
2000	349	16:52:16	o6baa2010	South	22.9528	No
2000	349	17:16:00	o6baa2ntq	South	37.9522	No
2000	349	17:27:00	o6baa2020	South	44.0837	No
2000	351	11:00:31	o6ba03010	North	111.6184	Yes

2000	351	11:25:51	o6ba03utq	North	127.7846	Yes
2000	351	12:19:14	o6ba03020	North	159.2104	Yes
2000	351	12:26:53	o6ba03uyq	North	163.7852	Yes
2000	351	13:56:14	o6ba03v4q	North	217.907	Yes
2000	351	14:00:37	o6ba03030	North	220.406	Yes
2000	351	14:27:44	o6ba03vhq	North	237.7122	Yes
2000	351	14:38:44	o6ba03040	North	243.4514	Yes
2000	351	15:29:38	o6ba03vmq	North	274.3524	No
2000	351	17:08:42	o6baa3010	South	334.2355	No
2000	351	17:30:12	o6baa3w3q	South	347.6957	Yes
2000	351	17:40:12	o6baa3020	South	353.3171	No
2000	353	9:27:49	o6ba04010	South	356.8136	No
2000	353	9:53:09	o6ba04boq	South	12.7257	No
2000	353	10:04:09	o6ba04020	South	18.7806	No
2000	353	10:54:02	o6ba04btq	South	48.966	Yes
2000	353	11:34:19	o6ba04bzb	South	73.3211	Yes
2000	353	12:30:29	o6ba04030	South	107.2026	Yes
2000	353	14:09:59	o6baa4chq	North	167.3598	Yes
2000	353	14:48:57	o6baa4cnq	North	190.9592	Yes
2000	353	15:43:22	o6baa4010	North	223.7685	Yes
2000	353	16:21:29	o6baa4020	North	246.8136	Yes
2000	363	7:07:20	o6ba01o1q	South	337.8215	No
2000	363	7:49:39	o6ba01o7q	South	3.5056	No
2000	363	8:43:44	o6ba01030	South	36.102	No
2000	363	9:15:18	o6ba01olq	South	55.7924	No
2000	363	9:26:18	o6ba01onq	South	61.7811	No
2000	363	10:23:12	o6baa1opq	South	96.2163	No
2000	363	11:59:10	o6bab1010	North	154.3189	No
2000	363	12:20:40	o6bab1p6q	North	167.9586	No
2000	363	12:30:40	o6bab1020	North	173.3996	No
2001	13	16:50:08	o6ba06ryq	North	218.8244	No
2001	13	17:29:44	o6ba06s4q	North	242.7634	Yes
2001	13	18:19:38	o6ba06010	North	272.9895	Yes
2001	13	19:58:39	o6baa6smq	South	332.8875	No
2001	13	20:38:36	o6baa6suq	South	357.0381	Yes
2001	13	21:32:26	o6baa6010	South	29.5412	Yes
2001	13	22:04:00	o6baa6t8q	South	49.2932	Yes
2001	13	22:15:00	o6baa6taq	South	55.2182	Yes
2001	13	22:18:52	o6baa6tcq	South	57.6514	Yes
2001	13	23:44:40	o6baa6tiq	South	109.5193	Yes
2001	20	12:41:34	o6ba07wuq	South	42.04	Yes

2001	20	13:21:10	o6ba07x0q	South	65.9783	Yes
2001	20	14:11:08	o6ba07010	South	96.2437	No
2001	20	14:42:42	o6ba07xeq	South	116.1648	No
2001	20	14:53:42	o6ba07xgq	South	121.9198	No
2001	20	15:50:07	o6baa7xiq	North	156.1195	Yes
2001	20	16:30:04	o6baa7xqq	North	180.2693	No
2001	20	17:23:53	o6baa7010	North	212.7613	No
2001	20	17:55:27	o6baa7y4q	North	232.6127	Yes
2001	20	18:06:27	o6baa7y6q	North	238.4375	Yes
2001	20	19:43:31	o6bab7yeq	South	297.0287	No
2001	21	16:00:04	o6ba05aaq	South	312.5132	Yes
2001	21	16:39:40	o6ba05agq	South	336.4513	Yes
2001	21	17:29:32	o6ba05010	South	6.6561	Yes
2001	21	18:01:06	o6ba05auq	South	26.514	Yes
2001	21	18:12:06	o6ba05awq	South	32.3322	Yes
2001	21	18:15:58	o6ba05ayq	South	34.7653	Yes
2001	21	19:41:45	o6ba05b4q	South	86.6211	Yes
2001	21	22:21:17	o6baa5bmq	North	183.0587	Yes
2001	21	23:01:14	o6baa5buq	North	207.2083	No
2001	32	8:56:31	o43b22lxq	North	272.566	No
2001	32	9:06:32	o43b22010	North	277.5126	No

Galileo radial	Galileo Local	HST Program
22.9208	19.985	7308
23.1049	20.0133	7308
23.5899	20.086	7308
23.5899	20.086	7308
81.103	0.9636	7308
81.103	0.9636	7308
No Galileo in	No Galileo in	7308
No Galileo in	No Galileo in	7308
55.059	21.588	7308
55.059	21.588	7308
55.2772	21.5967	7308
55.4946	21.6053	7308
98.3139	0.2839	7308
42.1848	20.3856	7308
42.1848	20.3856	7308
42.8245	20.4215	7308
40.3408	0.5991	7308
40.3408	0.5991	7308
43.2001	0.2382	8171
42.5781	0.2726	8171
42.5781	0.2726	8171
18.188	16.9963	8171
18.188	16.9963	8171
18.9336	17.135	8171
18.9336	17.135	8171
26.477	18.1638	7769
26.6847	18.1845	7769
26.6847	18.1845	7769
27.2997	18.2448	7769
27.2997	18.2448	7769
27.2997	18.2448	7769
27.7148	18.2845	7769
28.1258	18.323	7769
28.1258	18.323	7769
36.6506	18.9854	7769
36.6506	18.9854	7769
36.6506	18.9854	7769
36.6506	18.9854	7769
36.9861	19.0074	7769
37.319	19.029	7769

37.9773	19.0711	7769
42.3204	19.3301	7769
42.3204	19.3301	7769
42.3204	19.3301	7769
42.3204	19.3301	7769
42.6141	19.3466	7769
42.9057	19.3629	7769
43.4828	19.3947	7769
43.7683	19.4104	7769
55.639	19.8138	8171
55.639	19.8138	8171
55.639	19.8138	8171
55.8328	19.8247	8171
55.8328	19.8247	8171
55.8328	19.8247	8171
56.0253	19.8357	8171
56.0253	19.8357	8171
56.0253	19.8357	8171
7.2384	12.7939	8171
7.9958	13.4632	8171
76.0187	19.8391	8171
76.0187	19.8391	8171
76.2369	19.8452	8171
6.5533	10.6917	8171
6.8066	11.1004	8171
218.6383	18.924	8171
218.3945	18.925	8171
218.3945	18.925	8171
115.767	19.5731	8657
115.767	19.5731	8657
115.5272	19.5755	8657
115.5272	19.5755	8657
115.0477	19.5804	8657
115.0477	19.5804	8657
115.0477	19.5804	8657
114.808	19.5829	8657
114.568	19.5853	8657
114.568	19.5853	8657
114.3289	19.5878	8657
114.3289	19.5878	8657
105.4073	19.6851	8657

105.4073	19.6851	8657
105.1688	19.6879	8657
105.1688	19.6879	8657
104.6907	19.6935	8657
104.6907	19.6935	8657
104.6907	19.6935	8657
104.6907	19.6935	8657
104.4524	19.6963	8657
103.9748	19.7019	8657
103.9748	19.7019	8657
103.9748	19.7019	8657
94.6815	19.8193	8657
94.6815	19.8193	8657
94.6815	19.8193	8657
94.4431	19.8225	8657
94.2059	19.8258	8657
93.9683	19.829	8657
93.4919	19.8356	8657
93.4919	19.8356	8657
93.2546	19.8388	8657
93.017	19.8421	8657
15.6328	23.7626	8657
15.2786	23.8517	8657
14.7537	23.9896	8657
14.5798	0.0373	8657
14.406	0.0862	8657
13.8959	0.237	8657
13.0697	0.5071	8657
12.908	0.5642	8657
12.908	0.5642	8657
115.1022	16.5974	8657
115.3387	16.6001	8657
115.3387	16.6001	8657
115.8125	16.6055	8657
115.8125	16.6055	8657
116.0499	16.6081	8657
116.0499	16.6081	8657
116.0499	16.6081	8657
116.0499	16.6081	8657
116.5243	16.6135	8657
141.4522	16.8636	8657

141.69	16.8658	8657
141.69	16.8658	8657
141.69	16.8658	8657
141.9273	16.8679	8657
141.9273	16.8679	8657
142.1649	16.87	8657
142.1649	16.87	8657
142.1649	16.87	8657
142.1649	16.87	8657
142.402	16.8722	8657
145.252	16.8976	8657
145.489	16.8997	8657
145.489	16.8997	8657
145.489	16.8997	8657
145.7264	16.9017	8657
145.7264	16.9017	8657
145.7264	16.9017	8657
146.2014	16.9059	8657
146.2014	16.9059	8657
174.9517	17.1423	7308
174.9517	17.1423	7308